Supplementary Information for

A Novel Liquid Flow Electrochromic Smart Window for All-year-round Dynamic Photothermal Regulation

Ya Huang[1], Shuangdui Wu[2], Siming Zhao[1], Zhenyu Guo[1], Zhuojing Zhao[1], Xueke Wu[1], Baoshun Wang[1], Fei Wang[1], Aike Xi[1], Fan Lan[1], Yunrui Li[1], Jiaqi Xu[1], Run Li[1], Yanlong Zhao[1], Rufan Zhang[1]*

[1]Beijing Key Laboratory of Green Chemical Reaction Engineering and Technology, Department of Chemical Engineering, Tsinghua University, Beijing 100084, China.
[2]Key Laboratory of Eco Planning & Green Building, Ministry of Education, Department of Building Science, Tsinghua University, Beijing 100084, China.

*Corresponding author. Email: zhangrufan@tsinghua.edu.cn

Supplementary Video S1. Color changes in a manufactured house composed of LF-ESWs switching between the cooling and heating modes.

Supplementary Video S2. Flammability test of pure glass fiber.

Supplementary Video S3. Flammability test of pure glass fiber after infiltration of Zn-TFMS-PC.

Supplementary Video S4. Flammability test of pure glass fiber after infiltration of Zn-TFMS-TEP.

Supplementary Video S5. Flammability test of pure glass fiber after infiltration of Zn-TFMS-PC/TEP.

Supplementary Text

Supplementary Text S1. Two simulations on the indoor temperature and indoor energy-saving capabilities.

To better explain the effect of electrochromic smart windows on the indoor temperature and energy consumption of buildings, we established two means for simulation, including temperature simulation (Supplementary Fig. S1) and energy consumption (Supplementary Fig. S2). Notably, the simulation is the ideal situation, without considering lighting energy consumption.

(1) A one-dimensional steady-state model. The heat transfer process was simplified to a one-dimensional steady-state model. Specifically, this model elucidates the quantitative interplay between indoor temperature, $T_{VIS+NIR}$, and ε_{MIR} of the window at a specific ambient temperature. The net radiation method was used to analyze the heat transfer effects of the windows. Supplementary Fig. S1 shows the heat transfer model in an indoor scenario with two heat transfer surfaces, *i.e.*, the outer surface of the window (Surface 1) and the inner surface of the window (Surface 2), and with two heat transfer environments, *i.e.*, the indoor environment and the ambient environment (Ambient 3). The inward and outward radiative heat fluxes were denoted as q_i and q_o, respectively. Besides, to show the effect of windows' absorption and transmission, the model assumed that the indoor air exclusively absorbs and transmits solar irradiation and infrared light with no reflection, adhering to the principle of conservation ($\tau+\varepsilon=1$).

According to the Stephen-Boltzmann and energy conservation laws, the energy balance equations for the two interfaces and indoor air are shown below.[1]

For the window's outer surface (Surface 1):

$$q_{i1}=q_{sun}+q_{rad,a} \tag{1-1}$$

$$q_{o1}=q_{rad,1}+q_{conv,1}+(1-\varepsilon_1)q_{rad,a}+\tau q_{sun}+q_{cond} \tag{1-2}$$

For the window's inner surface (Surface 2):

$$q_{i2}= q_{cond}+\tau q_{sun}+q_{rad,air} \tag{1-3}$$

$$q_{o2}=q_{rad,2}+q_{conv,2}+\tau q_{sun}+(1-\varepsilon_2)q_{rad,air} \tag{1-4}$$

For the indoor air (Ambient 3):

$$q_{i3}=\alpha_{air}\tau q_{sun}+\varepsilon_a q_{rad,2}+\varepsilon_a(1-\varepsilon_2)q_{rad,air}+q_{conv,2} \tag{1-5}$$

$$q_{03}=q_{rad,air} \tag{1-6}$$

When thermal equilibrium was reached, $q_{i1}=q_{01}$, $q_{i2}=q_{o2}$, $q_{i3}=q_{o3}$, where ε_1, ε_2, and ε_a are the MIR emissivity of the window's outer surface, window's inner surface, and the air (including indoor and atmosphere), respectively. τ is the transmissivity of the window's outer surface. T and σ are the Stefan-Boltzmann constant and temperature, respectively. α_{air} is the solar radiation absorption coefficient of the indoor air. And h is the convection coefficient. To precisely analyze the impact of $T_{VIS+NIR}$ and ε_{MIR} on indoor temperature, the window model is streamlined to a single-surface configuration, disregarding the window's self-absorption ($\tau q_{sun,out}=\tau q_{sun,in}$).

The heat transfer (q_{cond}) between the outer surface and the inner surface was mainly by conduction and the q_{cond} between windows with air (q_{conv}) was mainly by natural convection. According to the practical conditions, the thermal conductivity (k_{glass}) of the glass typically ranges from 0.4 to 1.4 W/(mK), which depends on its composition, density, and temperature. For computational simplicity, k_{glass} was set to be 1 W/(mK) and the width of the window (λ) was set at 1 cm. According to Fourier's law and Newton's cooling law, the resultant equations are derived as follows:

$$q_{conv,1}=h_{out}(T_{out}-T_{amb}) \tag{1-7}$$

$$q_{conv,2}=h_{in}(T_{in}-T_{air}) \tag{1-8}$$

$$q_{cond}=k_{glass}(T_{out}-T_{in})/\lambda \tag{1-9}$$

For the window's outer surface:

$$q_{i1}=q_{o1} \tag{1-10}$$

$$q_{sun}+q_{rad,a}=q_{rad,1}+q_{conv,1}+(1-\varepsilon_1)q_{rad,a}+\tau q_{sun}+q_{cond} \tag{1-11}$$

$$q_{sun}+\varepsilon_a\sigma T_{amb}^4=h_{out}(T_{out}-T_{amb})+k\frac{T_{out}-T_{in}}{\lambda}+\varepsilon_1\sigma T_{out}^4 \tag{1-12}$$

For the window's inner surface:

$$q_{i2}=q_{o2} \tag{1-13}$$

$$q_{cond}+\tau q_{sun}+q_{rad,air}=q_{rad,2}+q_{conv,2}+\tau q_{sun}+(1-\varepsilon_2)q_{rad,air} \tag{1-14}$$

3

$$k\frac{T_{out} - T_{in}}{\lambda} + \varepsilon_2\varepsilon_a\sigma T_{air}^4 = \varepsilon_2\sigma T_{in}^4 + h_{in}\left(T_{in} - T_{out}\right) \tag{1-15}$$

For the indoor air:

$$q_{i3} = q_{o3} \tag{1-16}$$

$$\alpha_{air}\tau q_{sun} + \varepsilon_a q_{rad,2} + \varepsilon_a(1-\varepsilon_2)q_{rad,air} + q_{conv,2} = q_{rad,air} \tag{1-17}$$

$$\alpha air\tau qsun + \varepsilon_a\varepsilon_2\sigma T_{in}^4 + \varepsilon_a(1 - \varepsilon 2)\sigma T_{air}^4 + h_{in}\left(T_{in} - T_{out}\right) = \varepsilon_a\sigma T_{air}^4 \tag{1-18}$$

In this work, we define h_{out}=10 W/ (m²·°C), h_{in}=1.5 W/ (m²·°C), q_{sun}=1000 W·m⁻² in summer, q_{sun}=600 W m⁻² in winter, T_{amb}=35 °C in summer, and T_{amb}=5 °C in winter. By solving these equations, we can establish a quantitative relationship between the $T_{VIS+NIR}$ and ε_{MIR} with indoor temperature (Supplementary Fig. S4). The findings suggest that for summer comfort, windows should exhibit low $T_{VIS+NIR}$ and high ε_{MIR}, while for winter warmth, high $T_{VIS+NIR}$ and low ε_{MIR} are preferable.

(2) Simulation of office building energy consumption without considering the lighting energy consumption. As mentioned above, $T_{VIS+NIR}$ and ε_{MIR} were chosen as two important indicators. A twelve-layer building model with a floor dimension of 73 m (length) × 49 m (Width) × 48 m (Height) and a window-to-wall ratio of 40% was constructed to calculate energy consumption (Supplementary Fig. S2), which was selected from the United States Department of Energy's Commercial Reference Building Models. The building glazing system has a total window area of 4,636 m². To simulate a real building, we used a heat-balance-based approach to address all the heat transfer effects on the building's interior and exterior surfaces. The governing equations (energy balance equations) between internal (room temperature) and external (ambient temperature based on meteorological data) surfaces were solved hourly throughout the year using the EnergyPlus software.

Beijing with four distinct seasons was selected for simulation. Employing standard glass as a reference, the simulation calculated the impact of varying the $T_{VIS+NIR}$ and ε_{MIR} on room energy consumption (Supplementary Fig. S5). For cooling purposes, an energy-saving effect is achieved only when the relationship between the $T_{VIS+NIR}$ and ε_{MIR} meets $\varepsilon_{MIR} > 2.21 T_{VIS+NIR} - 0.98$. The energy-saving effect reaches a summit when

the $T_{VIS+NIR}$ is low enough and the ε_{MIR} is high enough. Conversely, for the heating mode, energy savings are realized only when $\varepsilon_{MIR} < 0.74\ T_{VIS+NIR} + 0.21$. Here a better energy-saving effect is produced by a higher $T_{VIS+NIR}$ and a lower ε_{MIR}. These results demonstrate that the smart windows adapted to all seasons should realize a dynamic regulation of the VIS, NIR, and MIR bands, and the modulation range should be large enough to maximize the energy-saving efficiency.

The above two simulations were performed for indoor temperature and indoor energy consumption respectively, and the conclusions obtained from both approaches were consistent. However, the two simulations are too idealized and lack consideration of the real environment and the differences between different areas.

Supplementary Text S2. A simulation method for determining the optimal energy-saving regulation value in a given area.

Here, we proposed a simulation method in which the related factors such as the specific regional conditions, the lighting energy usage, *etc.*, were taken into consideration. A 5 m×5 m×3 m (width× depth × height) room was selected in the middle layer of the office building, as shown in Supplementary Fig. S3. Except for the south wall, the remaining walls are all adiabatic. South-facing windows have a 70% window-to-wall ratio. Therefore, when installing different types of windows in a south-facing orientation, the solar radiation and outdoor climate will have different impacts on the building temperature. The settings required for the building simulation are shown in Supplementary Table S1, including internal disturbances, schedules, and heating, ventilation, air conditioning, and refrigeration. Six cities with four distinct seasons were also selected for building simulation optimization.

The optimization process for multi-parameters is shown in Supplementary Fig. S6. The decisive variables, objective functions, optimization algorithms, and termination conditions were determined in the GenOpt tool. GenOpt could change the values of the decisive variables and generate a new EnergyPlus input file. The output of energy consumption calculated by EnergyPlus was imported into GenOpt to get the values of

the objective functions. When the energy consumption reached a minimum value, the operation was ended and an optimal solution was obtained. In this work, the variable parameters were also the $T_{VIS+NIR}$ and ε_{MIR} of the energy-saving windows in summer and winter.

Through the simulation optimization, we could answer the following questions.

In a city, what are the best setting values of $T_{VIS+NIR}$ and ε_{MIR} for smart windows to achieve the best energy-saving efficiency in summer and winter seasons, and how much energy can be saved compared with common windows?

In a city, what is the effective range of $T_{VIS+NIR}$ and ε_{MIR} for smart windows to achieve an energy-saving effect compared with common windows in summer and winter?

Based on the optimization program introduced before, we obtained the window characteristic parameters corresponding to the optimal energy-saving in summer and winter (shown in Fig. 1b and Supplementary Table S2). The optimization results showed that an optimal cooling effect in summer corresponded to a low transmittance ($T_{VIS+NIR}{\approx}0.3$) and a high MIR emissivity ($\varepsilon_{MIR}{\approx}1$). An ideal energy-saving smart window could save energy as much as 15-35% than normal windows in summer. For example, in Beijing, if the $T_{VIS+NIR}$ is lower than 0.659 and the ε_{MIR} is higher than 0.905, the smart windows will save more energy than common windows. The optimal values of energy savings are $T_{VIS+NIR}$=0.356 and ε_{MIR}=0.999. Besides, the optimization results showed that optimal heating in winter corresponded to a high solar emissivity ($T_{VIS+NIR}{\approx}0.65$) and a low MIR emissivity ($\varepsilon_{MIR}{\approx}0$). An energy-saving smart window could save energy as much as 13-28% more than common windows in winter. For example, in Beijing, if the $T_{VIS+NIR}$ is higher than 0.494 and the ε_{MIR} is lower than 0.256, the smart windows will save more energy than common windows. The optimal values of energy savings are $T_{VIS+NIR}$=0.684 and ε_{MIR}=0.001.

Supplementary Text S3. Cost-effectiveness of the LF-ESWs.

The prepared LF-ESW offers an innovative solution for energy savings and photothermal regulation. Assessing its cost-effectiveness is crucial to determine its practical viability. This analysis covers material costs, manufacturing expenses, the expected service life, energy savings, and economic viability while referencing market prices and sourcing data to support transparency. Overall, the LF-ESW features low material costs and a simple fabrication process. Materials like the zinc framework, CSA-doped PANI, and the PE protective layer provide excellent cost-effectiveness. Additionally, the incorporation of the liquid flow process improves electrochromic performance while keeping overall costs low. The fabrication process employs pulsed electrodeposition and modular assembly methods, which are not only efficient but also ensure stable product quality control. Considering these advantages, the LF-ESW demonstrates significant economic and practical feasibility for large-scale industrial applications.

1. Material Costs

Materials used in LF-ESWs include a zinc framework, a CSA-doped PANI film, a PE layer, the Zn-TFMS-PC/TEP electrolyte, and an FTO glass. Below are the estimated costs based on the data:

(1) Zinc framework: Zinc is a cost-effective alternative for the conductive electrode. Estimated price: ~$2–$5/m², based on Alibaba listings for industrial-grade zinc used in electrode fabrication. Source: Alibaba.

(2) CSA-doped PANI: This high-performance electrochromic material facilitates dynamic switching. Estimated cost: ~$5/m² for industrial-scale polymer synthesis, using data from comparable conducting polymers. Source: Chemical Sources International.

(3) Zn-TFMS-PC/TEP Electrolyte: PC: ~$0.02/gram, TEP: ~$0.08/gram. Source: Alibaba. Zn-TFMS: ~$0.10/gram. Source: Sigma-Aldrich.

(4) PE layer: PE provides durability and protection against environmental exposure. Estimated price: ~$0.05–$0.10/m². Source: Amazon.

(5) FTO glass. FTO glass serves as a transparent conductive substrate crucial for

electrochromic performance. Estimated cost: ~$10–$20/m², based on <u>Alibaba</u> for FTO-coated glass used in electrochromic and solar applications.

Based on the above, total estimated material costs for LF-ESWs are approximately $20–$33/m², depending on scaling and supply chain optimizations.

2. Manufacturing Costs

The LF-ESW leverages scalable and efficient manufacturing techniques, including pulsed electrodeposition, liquid flow process, integration, and assembly.

(1) Pulsed electrodeposition: Ensures uniform PANI deposition, minimizing material waste. Cost estimate: ~$3–$6/m² for equipment and process. Source: <u>SpringerLink</u>.

(2) Liquid flow process. The liquid flow process is unique to LF-ESW devices, enabling dynamic liquid electrolyte circulation to enhance MIR emissivity. This step involves microfluidic channel fabrication and pump integration. Microfluidic Channel Fabrication: Cost estimated at ~$5/m², based on industrial-scale polymer molding techniques. Source: <u>ScienceDirect</u>. Pump Integration: Includes small-scale pump installation to enable liquid flow. Cost estimate: ~$10 per pump. Source: <u>Alibaba Listings for Miniature Pumps</u>.

(3) Integration and Assembly: Involves combining layers (PE, Zinc framework, PANI, electrolyte, and conductive framework). Estimated cost: ~$8/m². Source: <u>Industry Reports on Smart Window Assembly</u>.

Based on the above, the total manufacturing cost is approximately $16–$19/m², plus $10 per unit for pumps.

3. Expected Service Life and Durability

Durability is a key determinant of cost-effectiveness. LF-ESWs demonstrate robust long-term performance:

(1) CSA-doped PANI: The PANI maintains stability after 5,000 cycles with only a 5% decay. Assuming 8 heating or cooling mode switches per year, 5000 cycles would equate to a lifespan of 600 years under such usage conditions. Besides, the performance of the smart window only declined by 18% after 6,000 cycles, Considering the actual situations, we conservatively estimate a functional lifespan

of at least 30 years.

(2) Zn-TFMS-PC/TEP Electrolyte: The electrolyte offers exceptional thermal stability (-100 °C to 150 °C) and non-flammability, ensuring operational safety in diverse climates while providing long-term stability for extended use.

   With minimal maintenance, the LF-ESWs' service life is expected to exceed 30 years, rivaling standard low-E glass systems.

4. Energy Savings and Economic Viability

   After a thorough analysis of the simulation results and a comprehensive consideration of key parameters, including the coefficient of performance (COP), the final energy efficiency data was obtained. Compared with existing literature on energy performance, our smart window has exhibited superior energy efficiency. The LF-ESWs could significantly save up to 86.35 MJ/m² annually compared with common glass and up to 49.532 MJ/m² versus low-E glass. Electricity costs vary by region and country, but the average cost in many parts of the world falls around $0.10/kWh.

$$1 \text{ kwh} = 3.6 \text{ MJ}$$

$$\text{Cost per MJ} = \frac{\text{Cost per kWh}}{3.6} = \frac{0.1}{3.6} = 0.028 \text{ USD/MJ}$$

   Assuming an energy cost of $0.028/MJ, this translates to annual savings of $2.4178/m² compared with common glass. Over a 30-year lifespan, energy savings reach $72.534/m², offering a high return on investment given the total material and manufacturing costs.

   In conclusion, the LF-ESWs represent a cost-effective and energy-efficient innovation for smart windows. By incorporating cost-saving strategies and leveraging its significant energy-saving potential, the LF-ESWs can achieve economic viability. Continuous optimization of materials and manufacturing processes, while maintaining high performance, will be key to scaling up the technology.

Supplementary Text S4. The perspective of both the carbon and environmental impact of the LE-ESWs.

1. Carbon Impact.

The carbon emission factor (CEF) is the amount of CO_2 emitted per unit of energy consumed. Common CEFs for various energy sources are shown below and are derived from the Intergovernmental Panel on Climate Change (IPCC) Emission Factor Database, available at Our World in Data, and the IPCC Guidelines for National Greenhouse Gas Inventories, accessible at IPCC NGGIP Website.

Coal-based electricity: ~0.094 kg CO_2/MJ

Natural gas-based electricity: ~0.056 kg CO_2/MJ

Grid electricity (global average):　~0.132 kg CO_2/MJ (This is influenced by the mix of energy sources used in power generation. The high CEF for grid electricity reflects a substantial contribution from fossil fuels like coal and natural gas, which are prevalent in many regions. CEFs depend on the energy mix of the region. Renewable-dominated grids (*e.g.*, Norway) have much lower CEFs (~0.01–0.1 kg CO_2/MJ).)

For this analysis, let's assume a grid electricity CEF of 0.094 kg CO_2/MJ, corresponding to coal-dominated energy production.

(1) The reduction in CO_2 emissions is calculated using:

$$CO_2 \text{ Reduction} = \text{Energy Savings} \times \text{CEF}$$

(2) CO_2 reduction compared with common glass:

$$86.35 \text{ MJ/m}^2/\text{year} \times 0.094 \text{ kg } CO_2/\text{MJ} = 8.1169 \text{ Kg } CO_2/\text{m}^2/\text{year}$$

(3) CO_2 reduction compared with Low-E glass:

$$49.532 \text{ MJ/m}^2/\text{year} \times 0.094 \text{ kg } CO_2/\text{MJ} = 4.656 \text{ Kg } CO_2/\text{m}^2/\text{year}$$

(4) CO_2 reduction for a 500 m^2 building compared with common glass:

$$8.1169 \text{ Kg } CO_2/\text{m}^2/\text{year} \times 500 \text{ m}^2 = 4058.45 \text{ kg } CO_2/\text{year} = 4.06 \text{ tons } CO_2/\text{year}$$

(5) CO_2 reduction for a 500 m^2 building compared with Low-E glass:

$$4.656 \text{ Kg } CO_2/\text{m}^2/\text{year} \times 500 \text{ m}^2 = 2328.0 \text{ kg } CO_2/\text{year} = 2.33 \text{ tons } CO_2/\text{year}$$

(6) CO_2 reduction over 30 years for a 500 m^2 building compared with common glass:

$$4058.45 \text{ kg } CO_2/\text{year} \times 30 \text{ years} = 121.75 \text{ tons } CO_2$$

(7) CO_2 reduction over 30 years for a 500 m^2 building compared with Low-E glass:

$$2328.0 \text{ kg } CO_2/\text{year} \times 30 \text{ years} = 69.84 \text{ tons } CO_2$$

2. Environmental Impact.

The LF-ESW consists of a zinc framework, an electrolyte, a PANI electrochromic material, and an FTO conductive glass. Both zinc framework and conductive glass are widely available, environmentally safe, and recyclable. Therefore, the focus of our environmental sustainability analysis is on the PANI material and the electrolyte.

2.1 PANI electrochromic material

PANI exhibits renewable and non-toxic properties, aligning with the principles of green chemistry.[2-4] Based on the principles of green chemistry, the following aspects highlight the environmentally friendly characteristics of PANI films:

(1) Utilization of Renewable Feedstocks (Principle 7)

PANI films are synthesized through the polymerization of aniline, which can be derived via green synthesis routes, such as bio-based aromatic compounds. Additionally, dopants like camphor sulfonic acid (CSA) can be extracted from natural camphor, further promoting the use of renewable resources.

(2) Reduction of Toxicity (Principle 3)

The synthesis of PANI films avoids the use of highly toxic chemicals. Instead, the electrochemical deposition process utilizes aqueous solutions as the reaction medium, eliminating the need for volatile organic solvents (VOCs). This minimizes environmental pollution and reduces potential health risks.

(3) Energy Efficiency (Principle 6)

PANI films are fabricated using low-temperature electrochemical deposition, which eliminates the need for energy-intensive thermal treatments, aligning with energy efficiency objectives. Moreover, the rapid response time of the films reduces energy consumption during their operational use.

(4) Renewability and Waste Minimization (Principles 10 & 1)

The degradation of PANI films is environmentally benign because waste materials can be recycled through chemical reduction or thermal decomposition. The resulting by-products exhibit low environmental toxicity, further contributing to sustainability

and waste reduction goals.

2.2 Electrolyte

The electrolyte was composed of PC, TEP, and Zn-TFMS. The three primary components of this electrolyte exhibit high boiling points and low volatility, resulting in significantly lower VOC emissions compared to traditional solvent systems such as methanol or ether. Additionally, the electrolyte demonstrates excellent stability under room and operating conditions, minimizing the risk of decomposition into toxic gases. Most importantly, all three substances have well-established post-treatment technologies. As a result, the electrolyte does not pose a risk to environmental sustainability.

(1) PC

Propylene carbonate has a high boiling point (242 °C), low volatility, and strong chemical stability, making it a safe solvent. It is widely used in lithium battery electrolytes and is considered a relatively low-toxicity solvent.[5] Waste electrolytes containing PC should be treated through recovery processes such as solvent redistillation or chemical neutralization.

(2) TEP

TEP is an efficient flame retardant with low volatility (boiling point of 215 °C) and low toxicity at typical concentrations (<30%). In the electrolyte, TEP enhances flame resistance, reducing the risk of fire. TEP has moderate biodegradability and should be treated to prevent direct discharge.[6] Recovery methods such as incineration or adsorption are effective. Given its typically low concentration in spent electrolytes, the environmental risk is manageable when properly handled.

(3) Zn-TFMS

Zn-TFMS is a commonly used zinc salt with good solubility and stability. It is relatively low in toxicity, but the trifluoromethane sulfonate anion may impose a burden on aquatic environments, suggesting careful management of waste materials. Zn-TFMS can be recovered through precipitation or ion-exchange processes, effectively reducing the long-term environmental impact of zinc and trifluoromethane sulfonate ions.

Overall, this LF-ESW is relatively safe and environmentally friendly. The materials selected are not only characterized by high safety and excellent stability, but also are equipped with comprehensive post-treatment and recycling technologies.
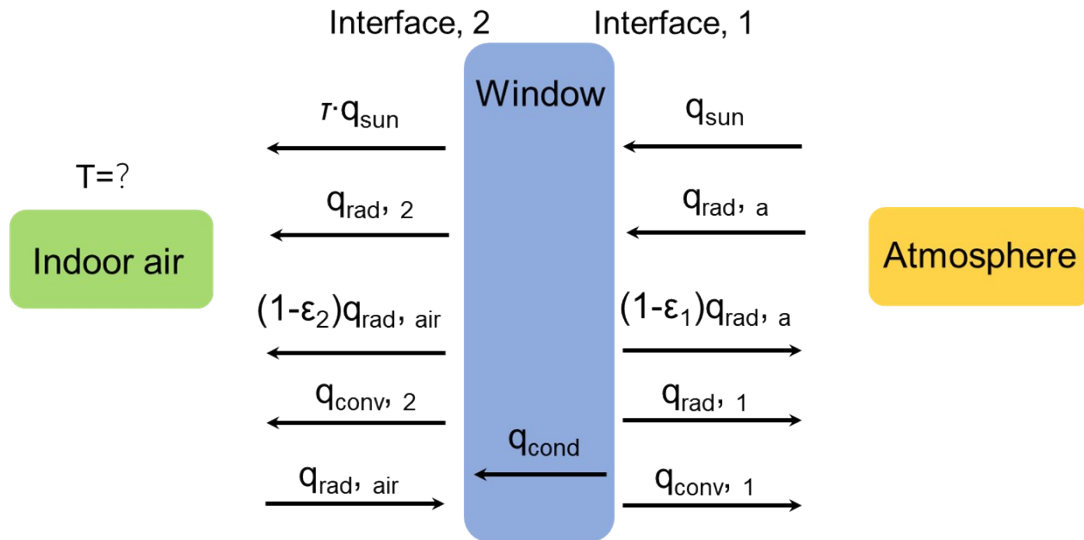
Supplementary Fig. S1. Window heat transfer model showing radiative heat transfer between the atmosphere and the interior of a room generated through a window.
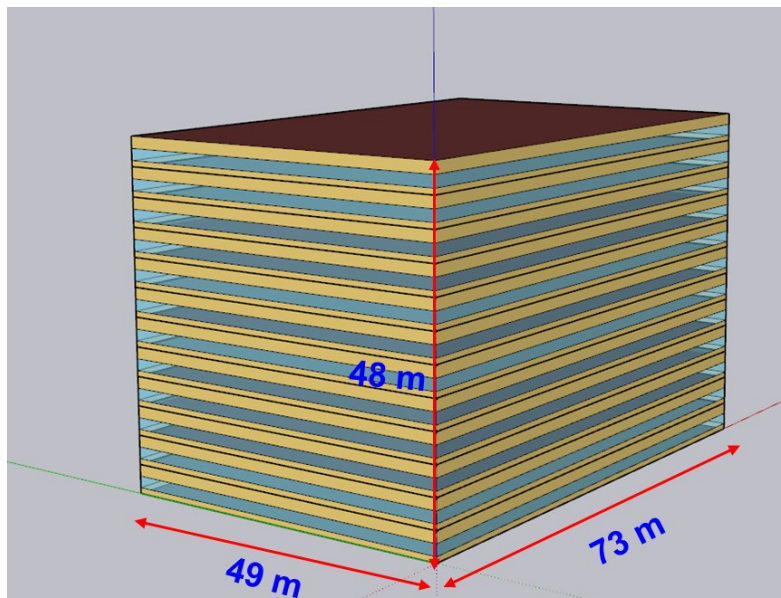
Supplementary Fig. S2. A 12-layer office building model with a window-to-wall ratio of 40% for the energy consumption simulation.
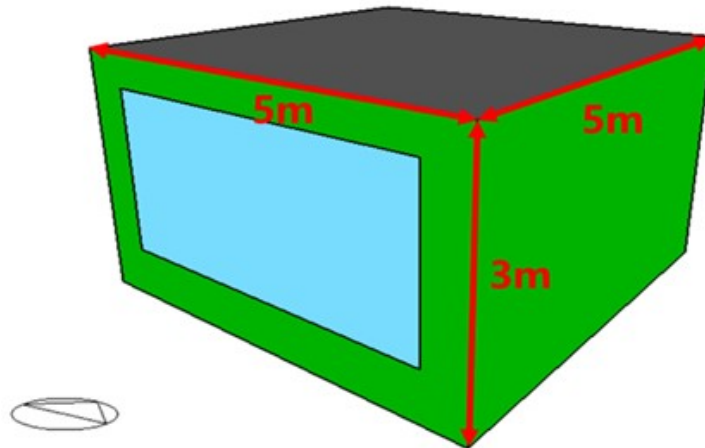
Supplementary Fig. S3. An office building simulation model with a window-to-wall ratio of 70% in the south-facing window.
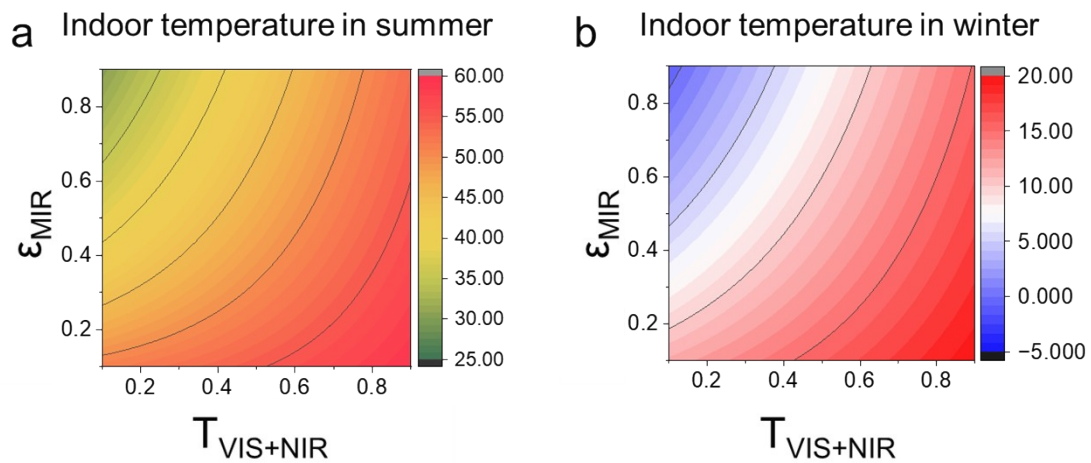
Supplementary Fig. S4. The effect on indoor temperature in summer (a) and winter (b) when varying the average $T_{VIS+NIR}$ and the average ε_{MIR}, respectively.
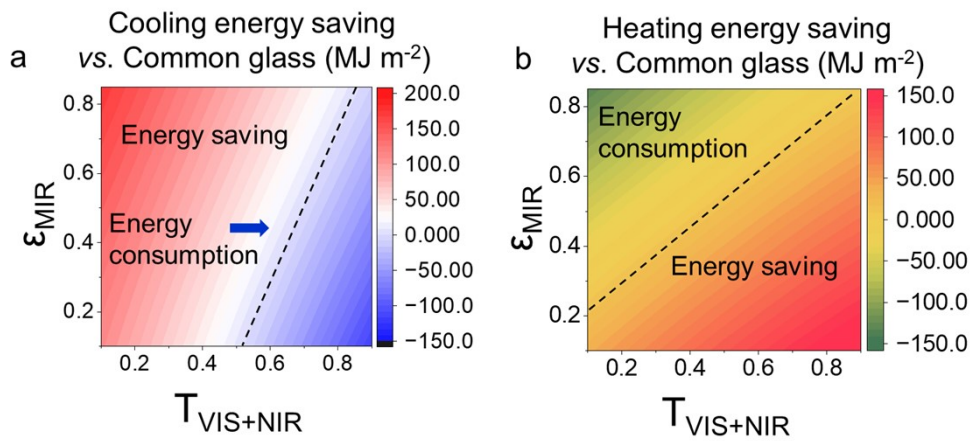
Supplementary Fig. S5. The effect on indoor energy savings in summer (a) and winter (b) when varying the average $T_{VIS+NIR}$ and the average ε_{MIR}, respectively.
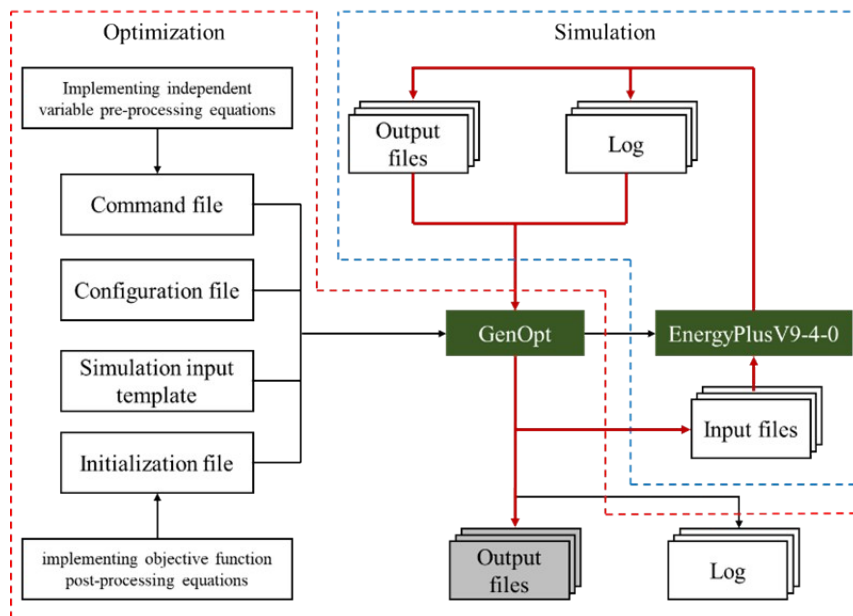
Supplementary Fig. S6. A multi-parameter optimization process to calculate the indoor energy consumption.

Emissivity vs. Conductivity (Hagen-Rubens Approximation)
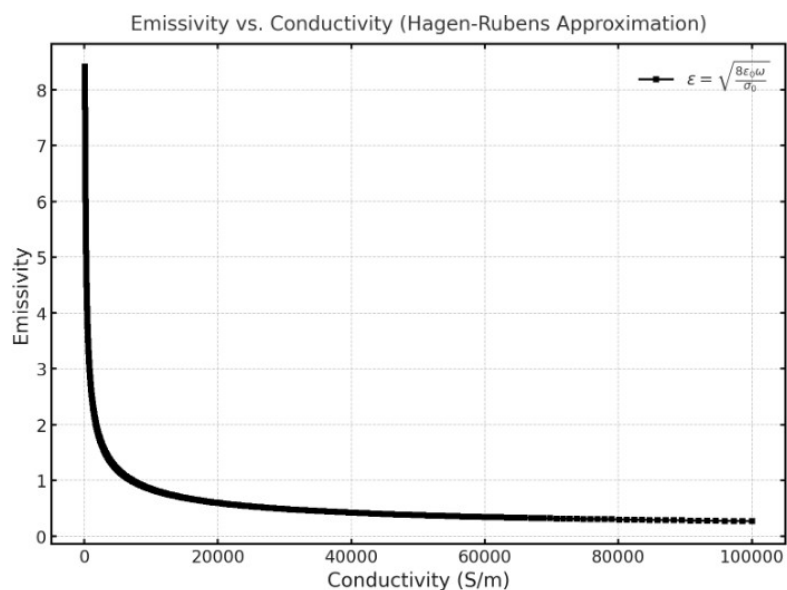
Supplementary Fig. S7. The Hagen-Rubens approximate theory about emissivity (ε)

and conductivity (σ).
$$\varepsilon = 1 - \rho = \frac{\sqrt{8\varepsilon_0\omega}}{\sigma 0}$$
, $\varepsilon_0 = 8.854 \times 10^{-12}$ F/m, $\omega = 10^{14}$ rad/s.

Solvents

EC PC DEC DMC EMC FEC MA EA MP DMSO

DOL DME DEGDME (G2) G3 TEGDME (G4) THF Me-THF

TEP TMP TPP DMF GLN AN DCM SN EG

Polymer matrices

PEO PMA PMMA PVDF-HFP PPC PVA PAN PolyDADMATFSI
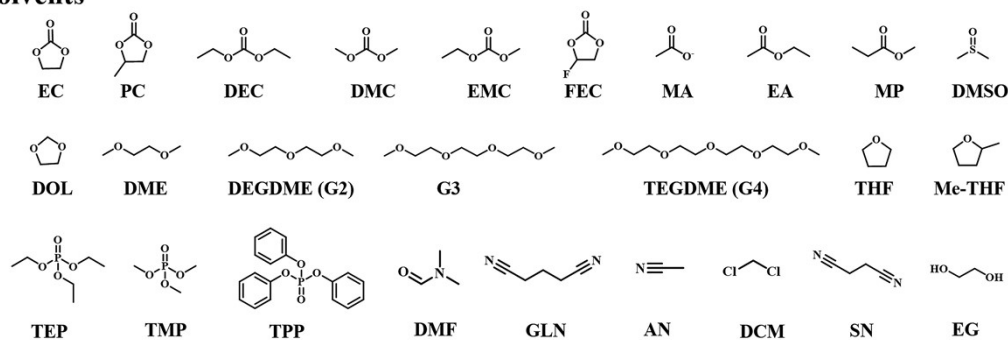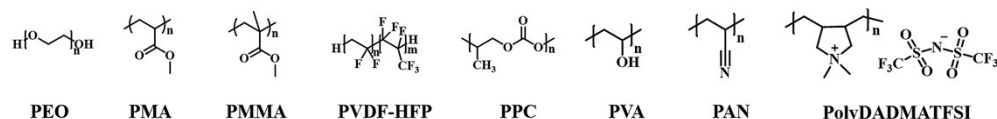
Sup

plementary Fig. S8. The commonly used electrolytes have high absorption

(emissivity) in the MIR band.[7]
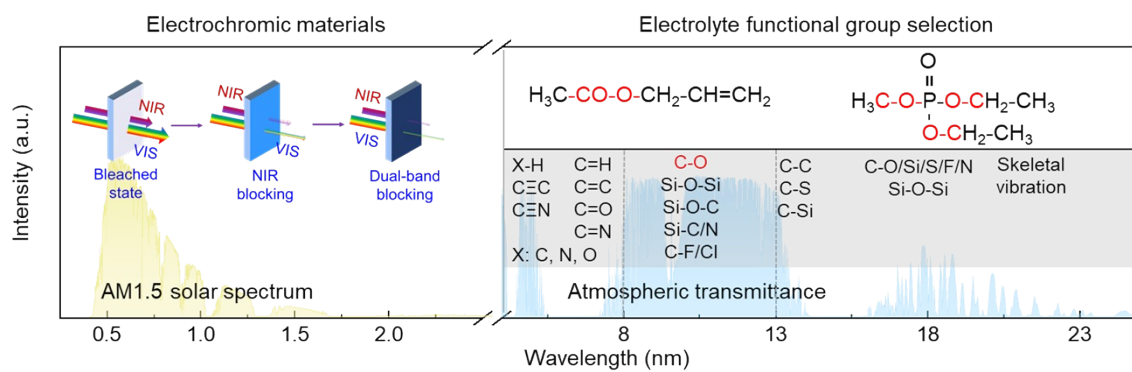
Supplementary Fig. S9. Mechanism of dual-band electrochromism and selection of electrolyte for multi-band smart windows.
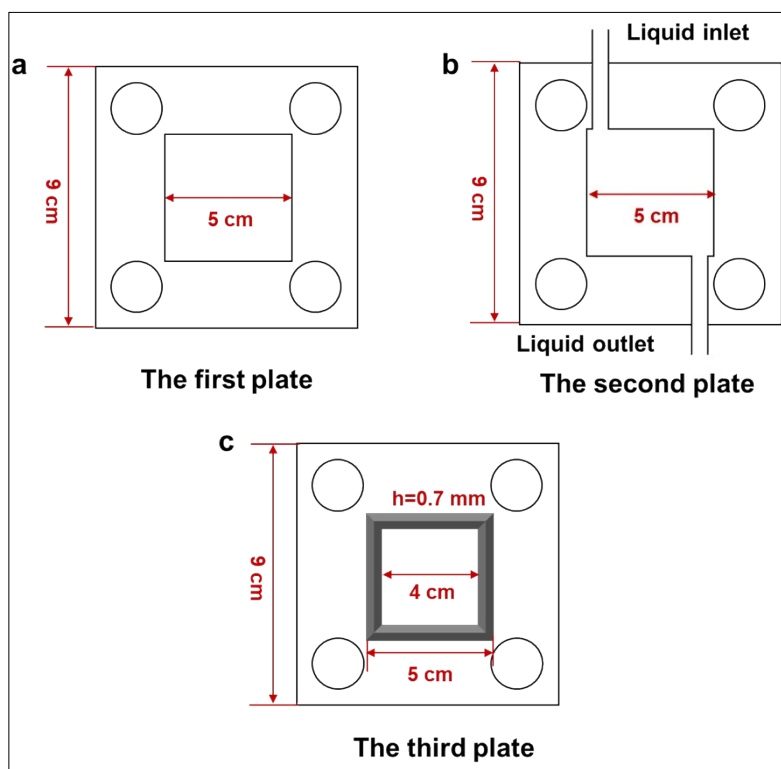
Supplementary Fig. S10. Design diagram of the LF-ESWs.
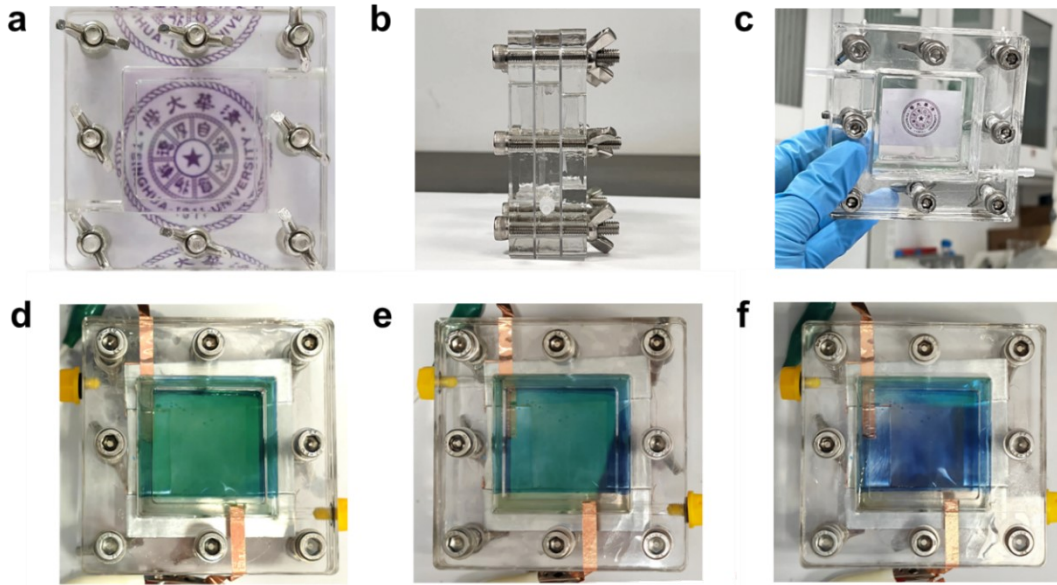
Supplementary Fig. S11. Demonstration of the prepared LF-ESWs. The size of the device is 9 cm×9 cm and the size of the electrochromic window is 5 cm×5 cm.
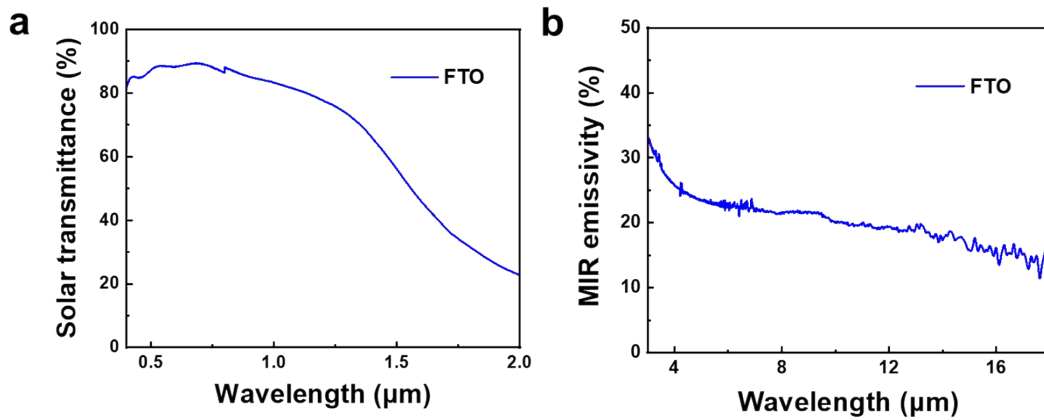
Supplementary Fig. S12. Spectral properties of FTO conductive glass.
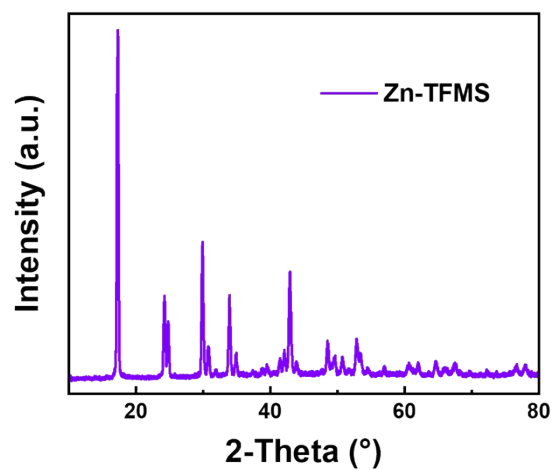
Supplementary Fig. S13. XRD results of the Zn-TFMS.
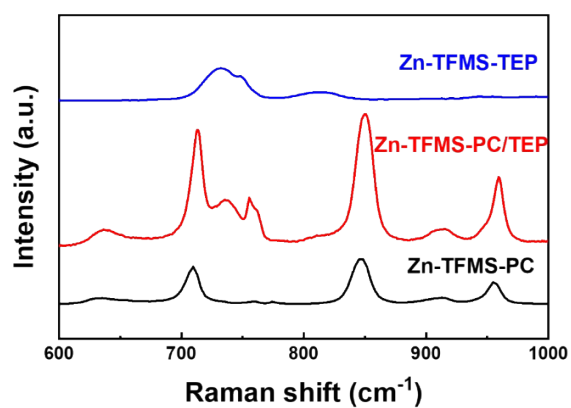
Supplementary Fig. S14. The Raman spectra of Zn-TFMS-PC, Zn-TFMS-TEP, and Zn-TFMS-PC/TEP.
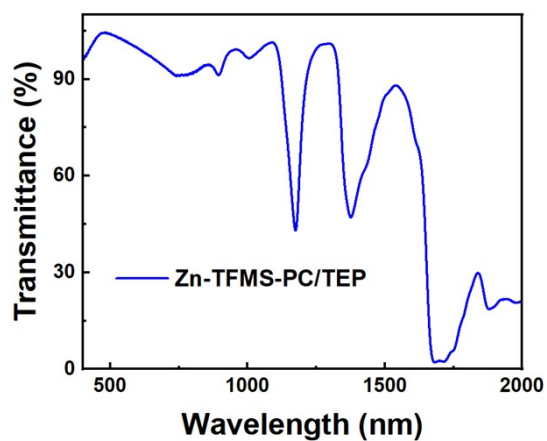
Supplementary Fig. S15. The transmittance curve of the Zn-TFMS-PC/TEP.
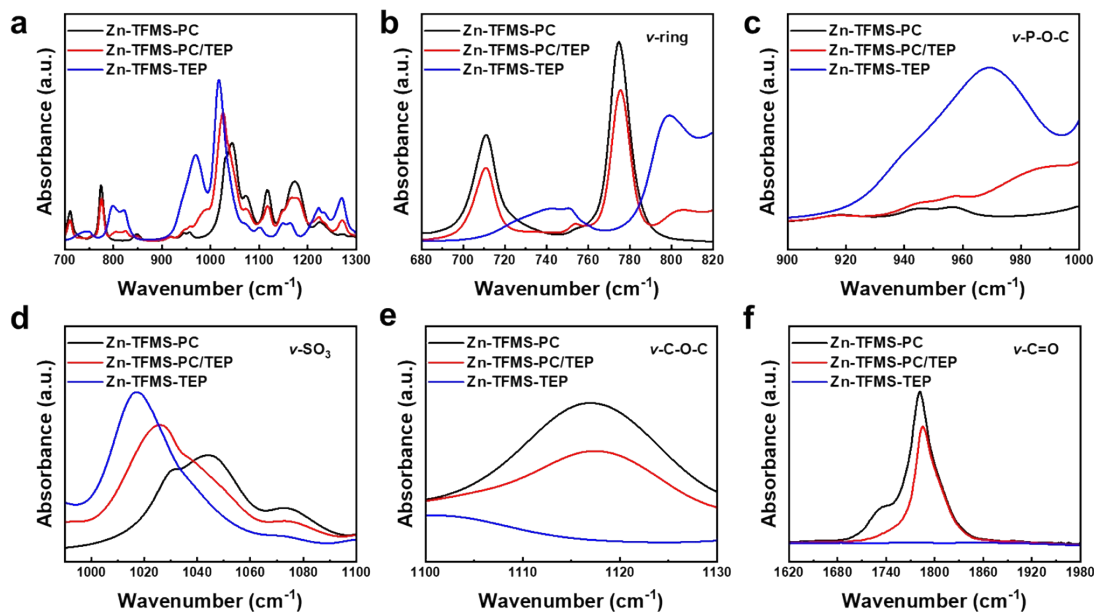
Supplementary Fig. S16. Chemical bonding vibrations of three electrolytes at 700-1300 cm^{-1}. The FTIR peaks at 985 cm^{-1} and 1100-1130 cm^{-1} were attributed to the P-O-C asymmetric stretching vibration and C-O-C stretch (v-C-O-C), respectively.[8] Interestingly, with the increased amount of TEP, the v-C-O-C decreased a little and moved to a higher frequency. That was because the TEP solvent had stronger chelation around Zn^{2+} and higher O donor density than the PC solvent, which also explained the increased solubility of Zn-TFMS in the electrolyte after the presence of TEP.[9]
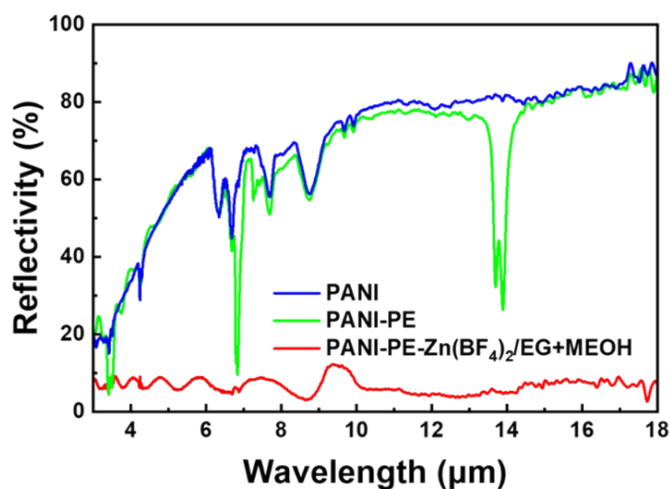
Supplementary Fig. S17. The modulation of MIR emissivity in different electrolytes.

Supplementary Fig. S18. Coin cells with the size of φ=15.6 mm assembled from two stainless steel tabs holding Zn-TFMS-PC/TEP electrolyte.
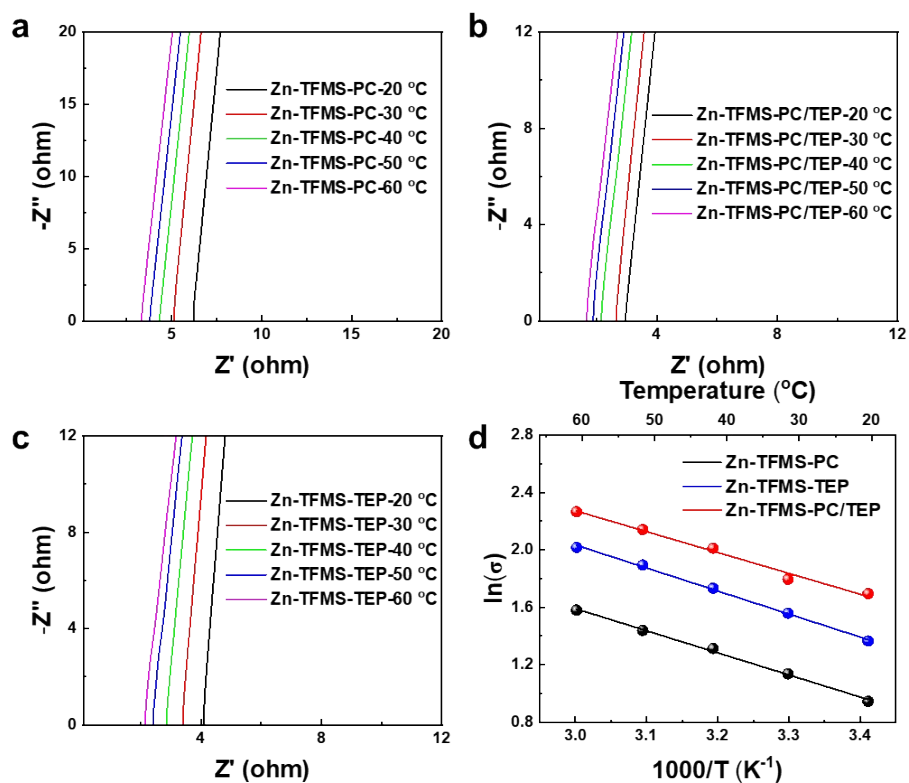
Supplementary Fig. S19. The impedance changes and the activation energies of Zn-TFMS-PC, Zn-TFMS-TEP, and Zn-TFMS-PC/TEP at different temperatures.
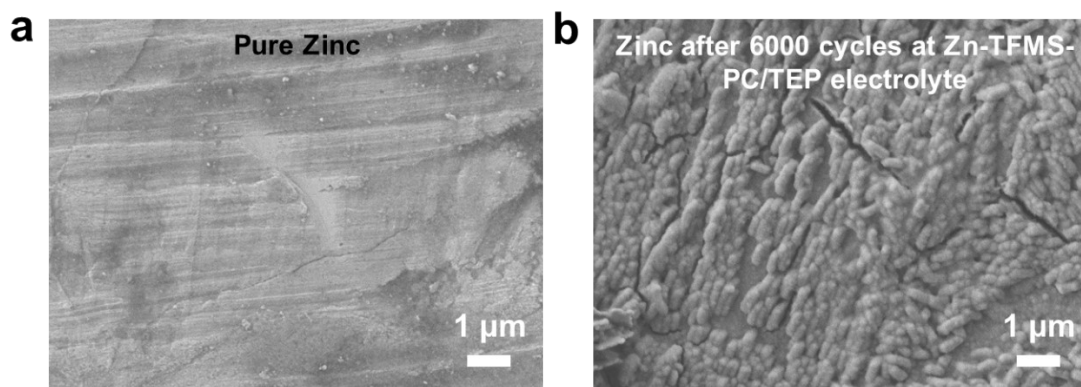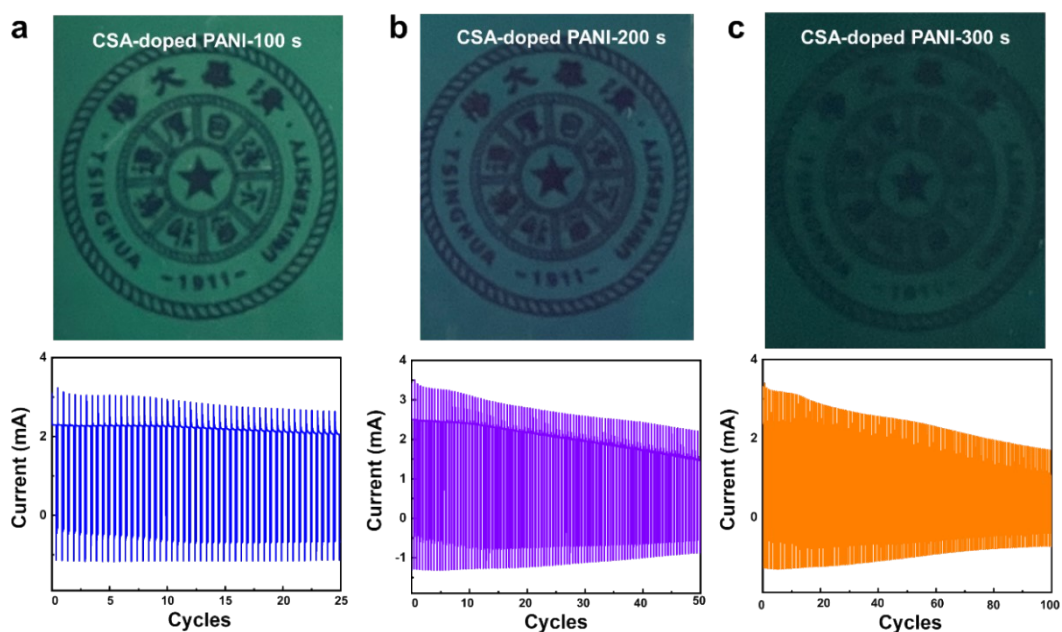
Supplementary Fig. S20. (a-b) The SEM of the pure Zinc and Zinc after 6000 cycles.
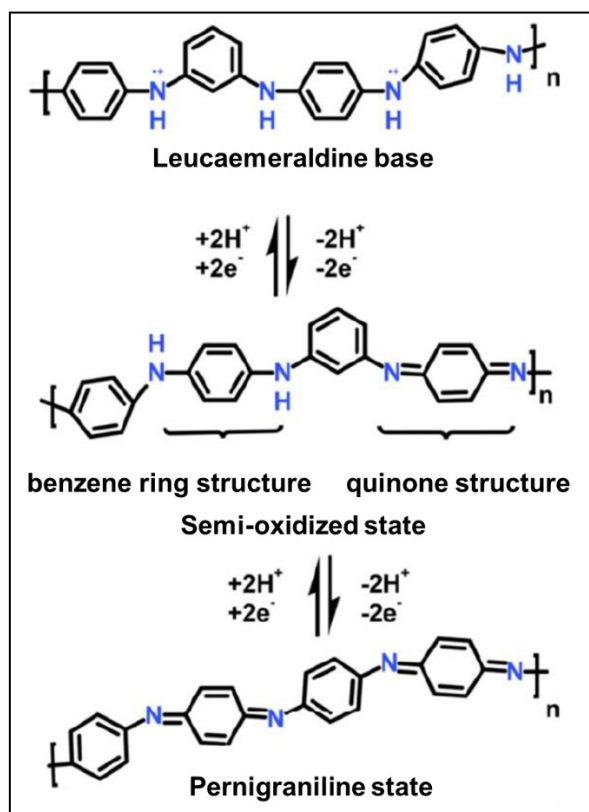

**Supplementary Fig. S21.** Molecular structure of PANI in different oxidation states.[10]
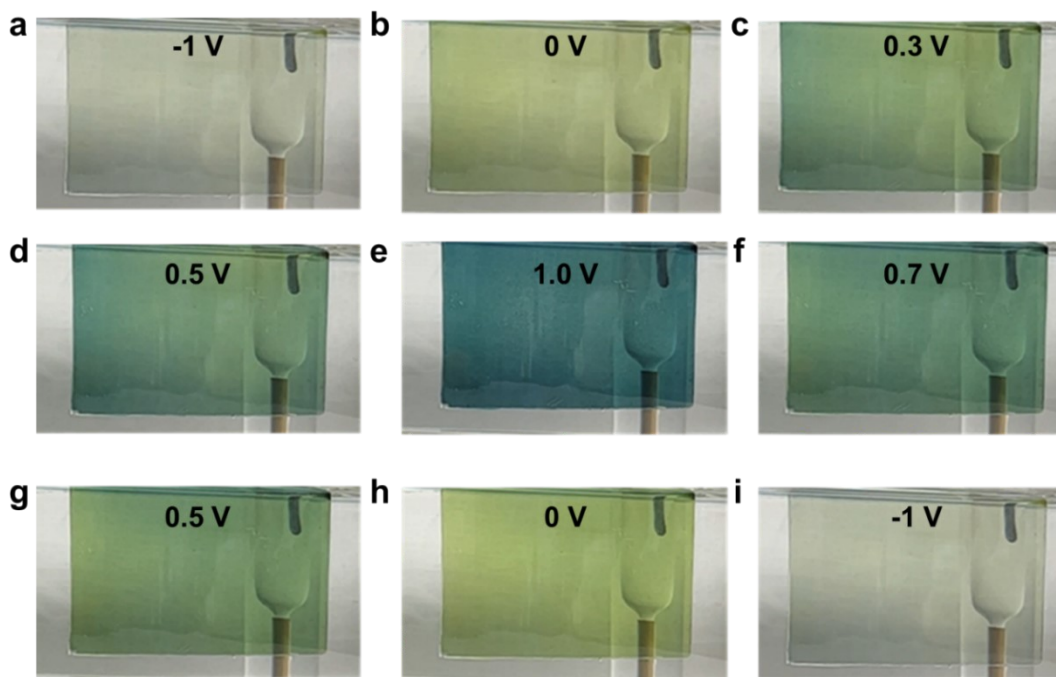
Supplementary Fig. S22. The color changes of CSA-doped PANI at different voltages.
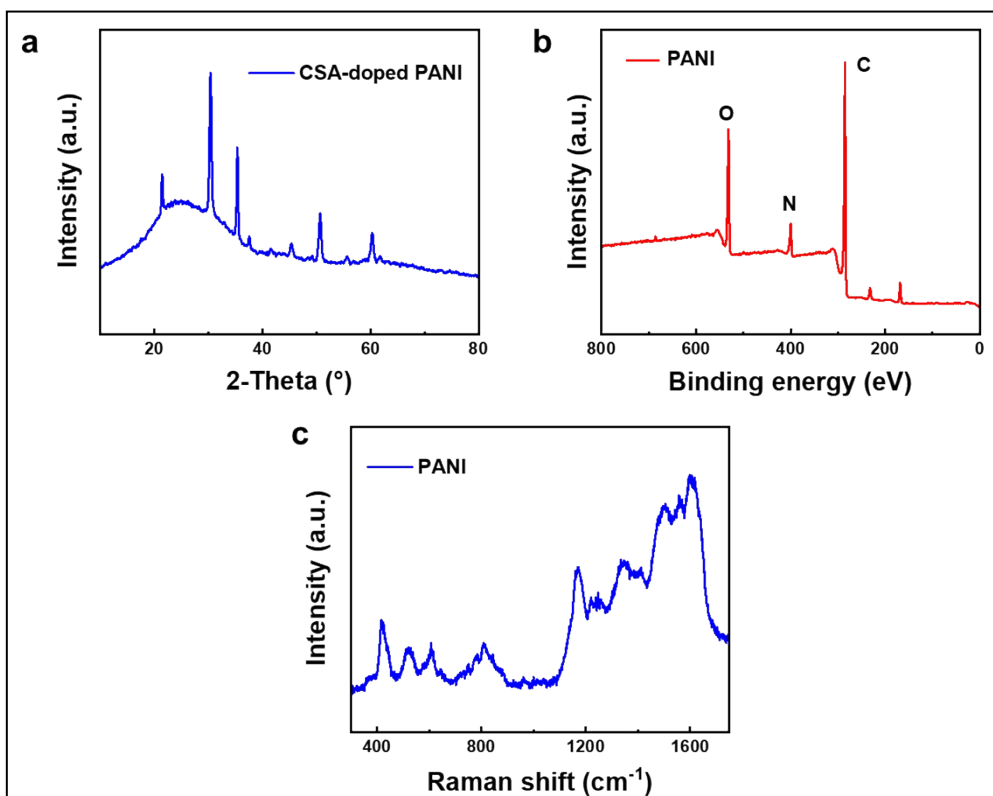

Supplementary Fig. S23. Different CSA-doped PANI films were obtained by controlling the different cycles in the electrochemical deposition processes. With an increase in the number of deposition cycles, the CSA-doped PANI films grow in thickness and darken in color. Consequently, the CSA-doped PANI-200s film was chosen as the target sample for its pronounced color change.
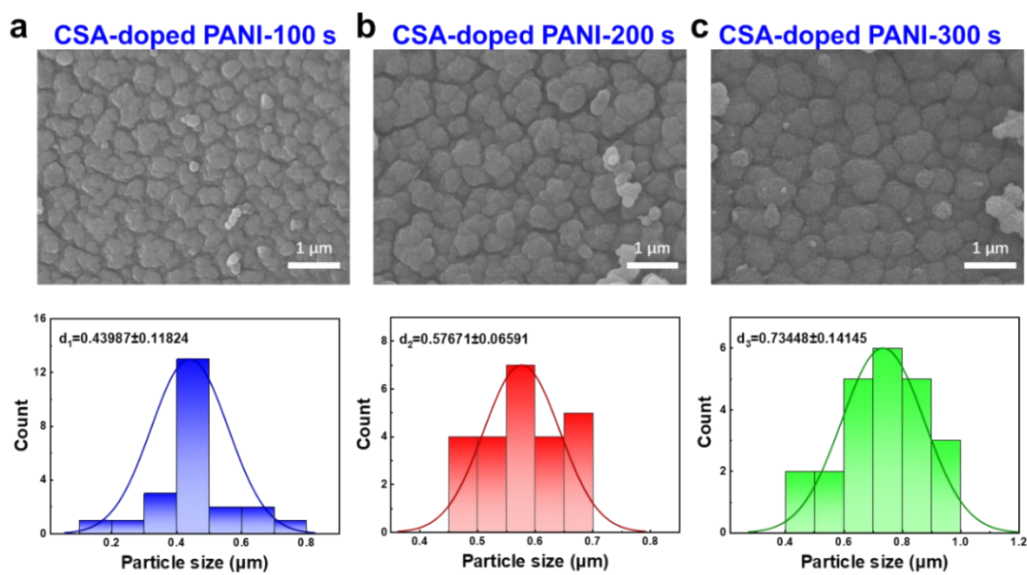
Supplementary Fig. S24. The SEM images and particle size statistics of the CSA-doped PANI at different cycles of electrodeposition. The size of the CSA-doped PANI particles increased with electrodeposition time.
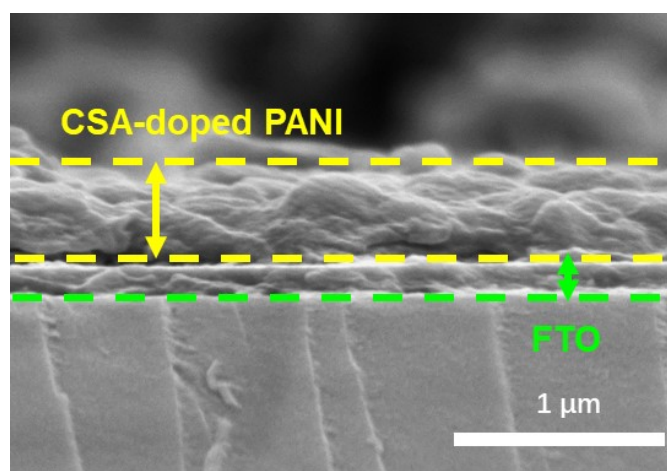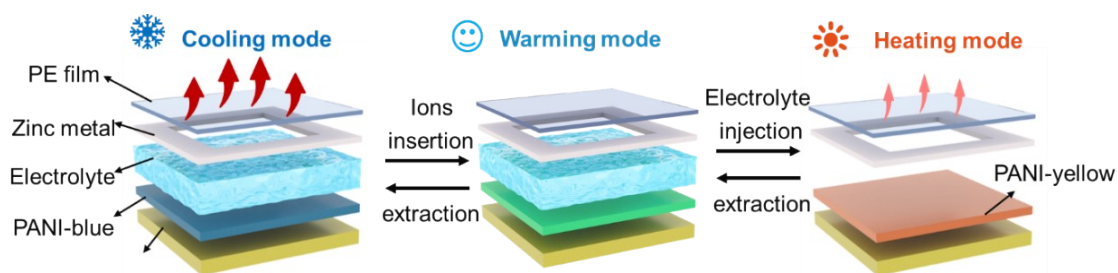

**Supplementary Fig. S25.** The SEM of the prepared CSA-doped PANI-200 s.

Supplementary Fig. S26. (a) XRD, (b) XPS, and (c) Raman results of the prepared CSA-doped PANI-200 s.
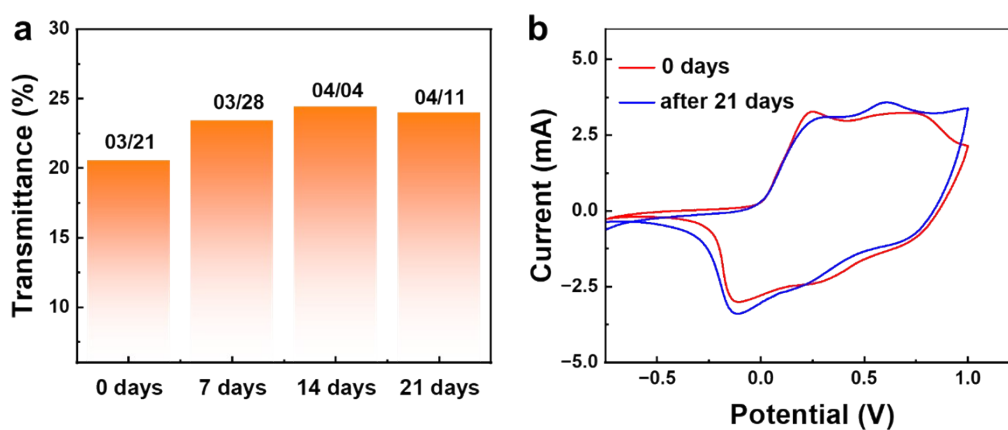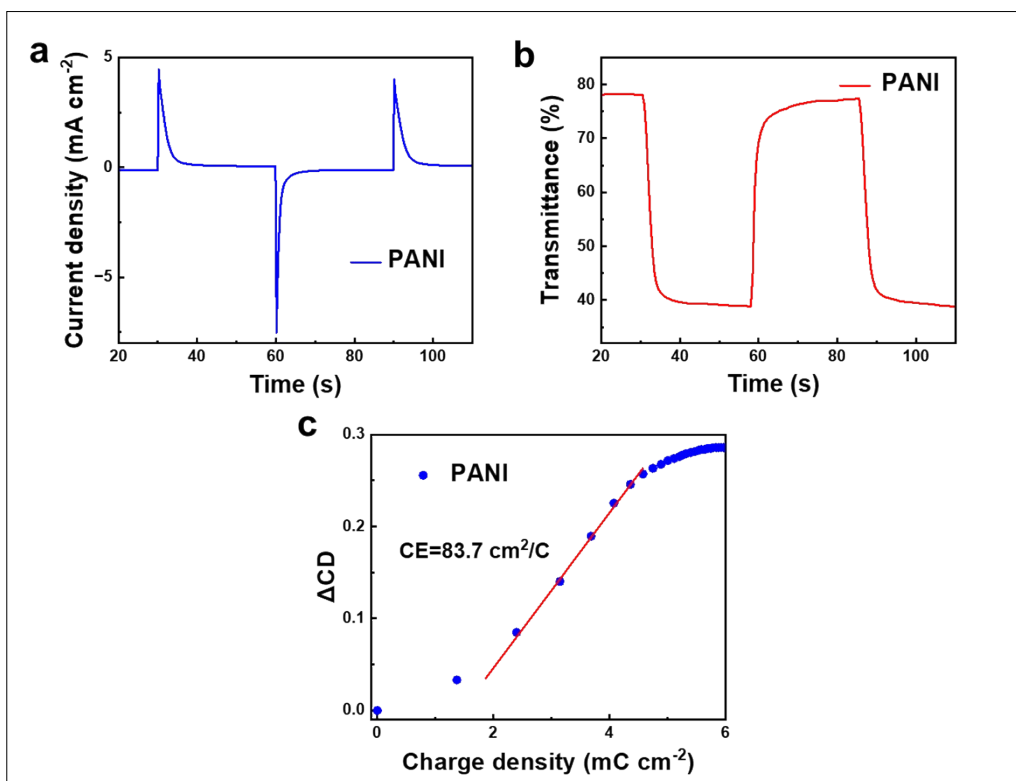

Supplementary Fig. S27. Transmittance and CV curves of the prepared CSA-doped PANI films before and after 21 days. Considering the test error, the data can reflect that its transmittance is basically unchanged.

**Supplementary Fig. S28.** The three switching states of the LF-ESWs.
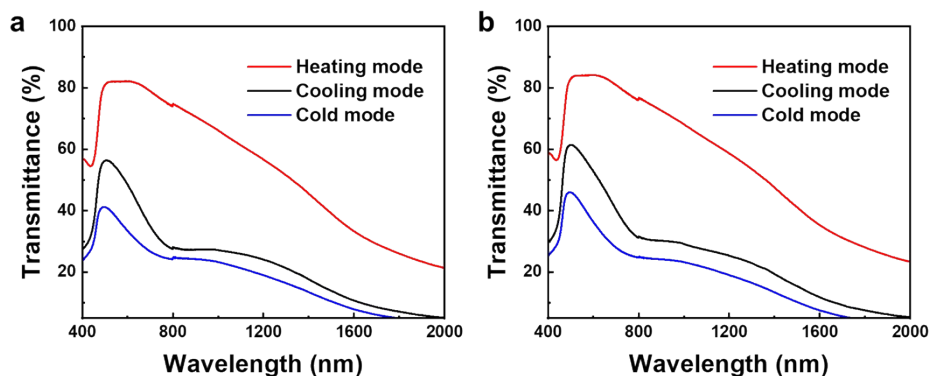
Supplementary Fig. S29. Transmittance curves of CSA-doped PANI films on FTO glass without electrolyte (a) and with electrolyte (b) at different voltages. It can be concluded that the electrolyte does not significantly affect the transmittance of the PANI.

Supplementary Fig. S30. (a-b) The response time of PANI film was measured by an electrochemical workstation coupled with a spectrometer. (c) The coloring efficiency of PANI film.
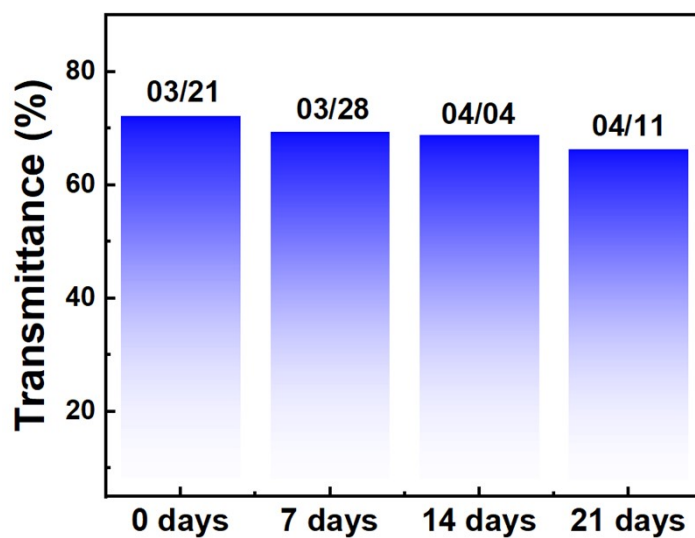

Supplementary Fig. S31. Transmittance of CSA-doped PANI films at yellow state before and after 21 days. Considering the test error, the data can reflect that its transmittance is basically unchanged.
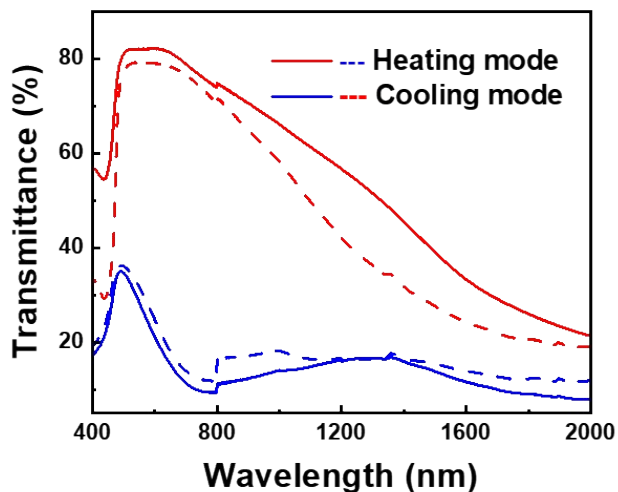
	Transmittance (Before cycling)	Transmittance (After cycling)
Heating mode	68.71%	61.06%
Cooling mode	17.57%	20.33%

Supplementary Fig. S32. The optical properties of PANI on FTO film before and after cycling.
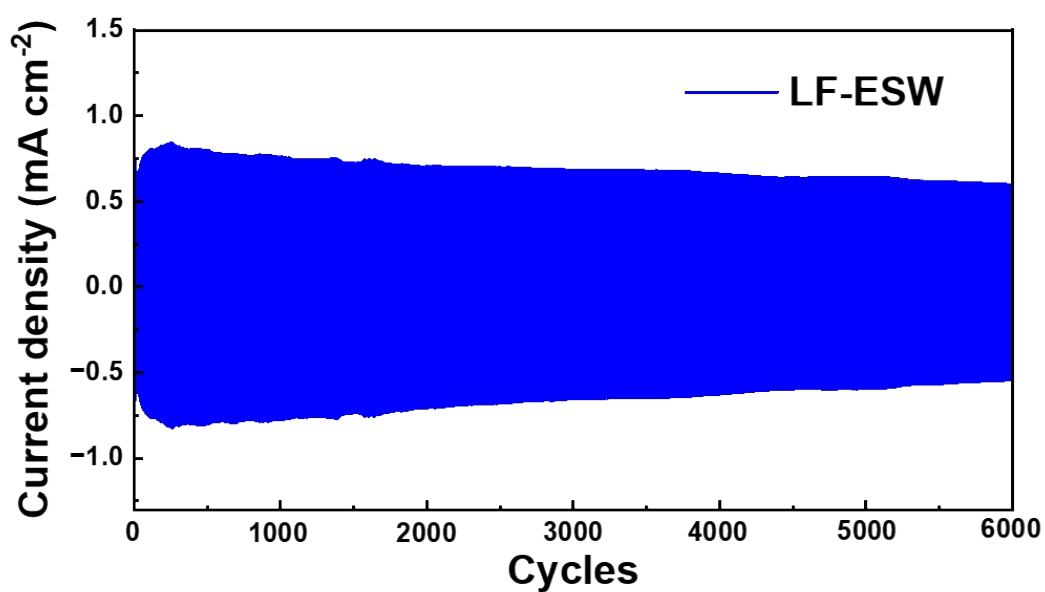
Supplementary Fig. S33. The long-term cycling test of LF-ESW.

low-E window

Supplementary Fig. S34. The optical photos of a low-E glass-based window with the size of 10 cm*10 cm.
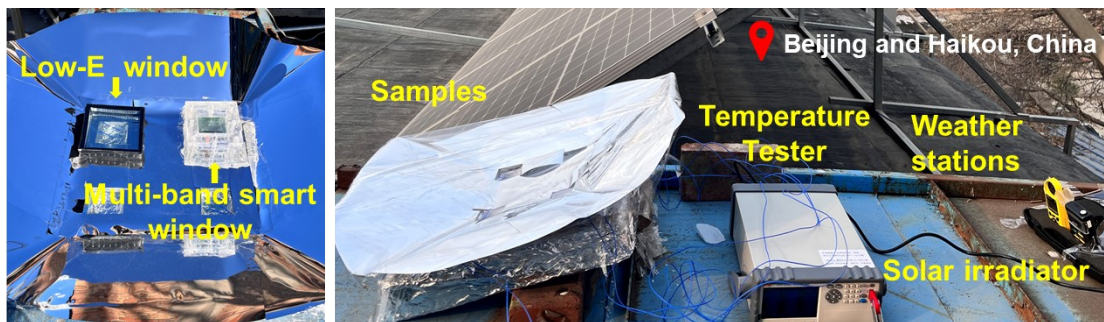
Supplementary Fig. S35. The simulation of the heating/warming/cooling performance of a house using LF-ESWs *vs*. low-E glass-based windows by standardized tests in Beijing, China, and Haikou, China, respectively. The standardized tests only consider the effect of the same size of the sample on the temperature of a fixed area.
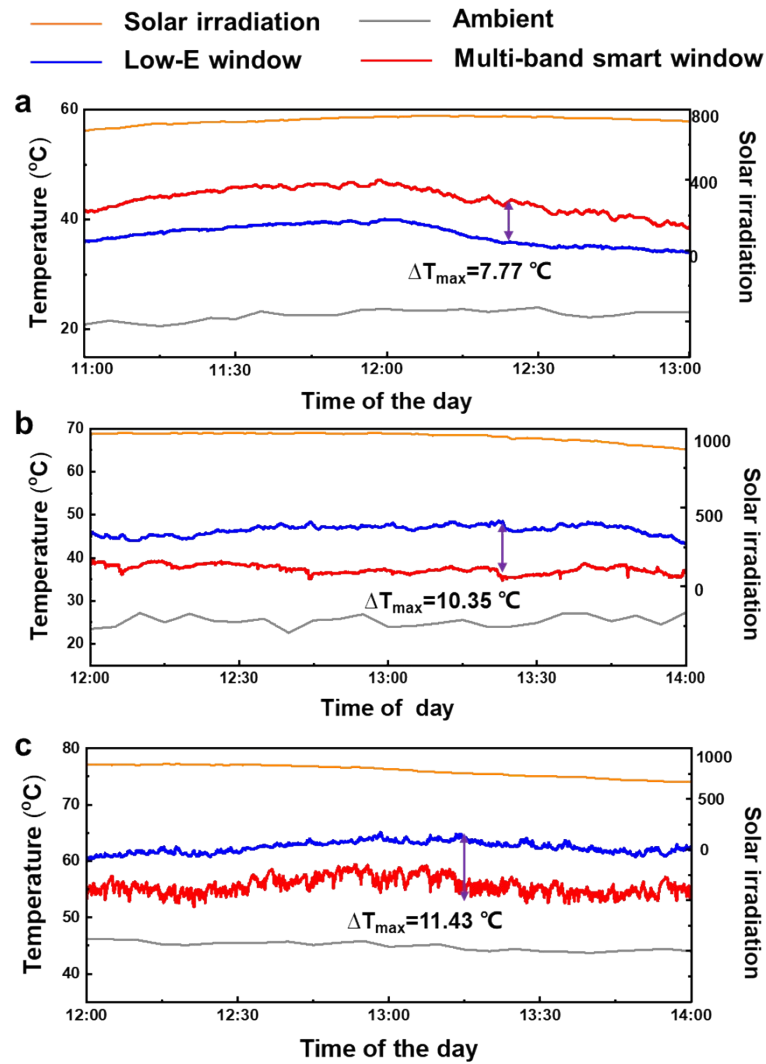
**Supplementary Fig. S36.** Temperature results of the LF-ESWs at (a) heating mode, (b) warming mode, and (c) cooling mode under standardized tests, respectively. In cold days, the LF-ESW can heat the interior temperature by up to 7.77 °C compared to Low-E glass-based windows from 11:00-13:00. In warm days, it can cool up to 10.35 °C cooler than Low-E glass-based windows from 12:00-14:00. In hot days, it can cool up to 11.43 °C cooler than Low-E glass-based windows from 12:00-14:00. The reason that the above values are larger than the temperature difference of the normalized test is that the room area of the standardized test is small and the heat circulation is poor.
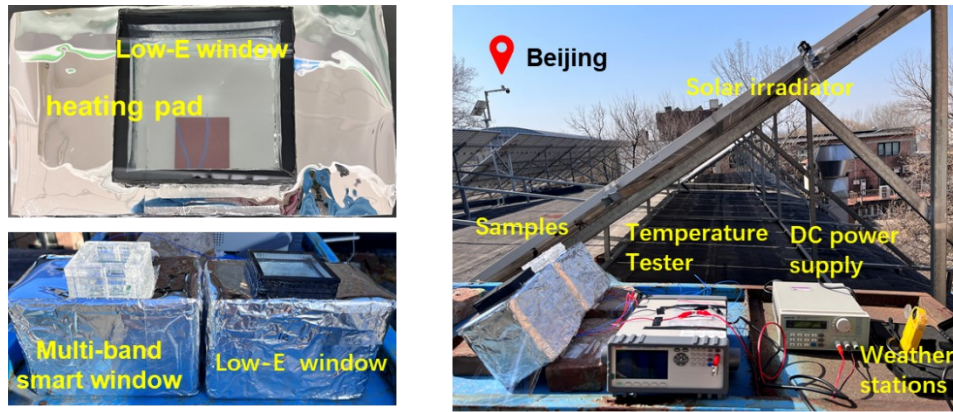
Supplementary Fig. S37. The simulation of the heating performance of a house using LF-ESWs *vs*. low-E glass-based windows by normalized tests in Beijing, China. The normalized test takes into account the window-to-wall ratio as well as the room size.
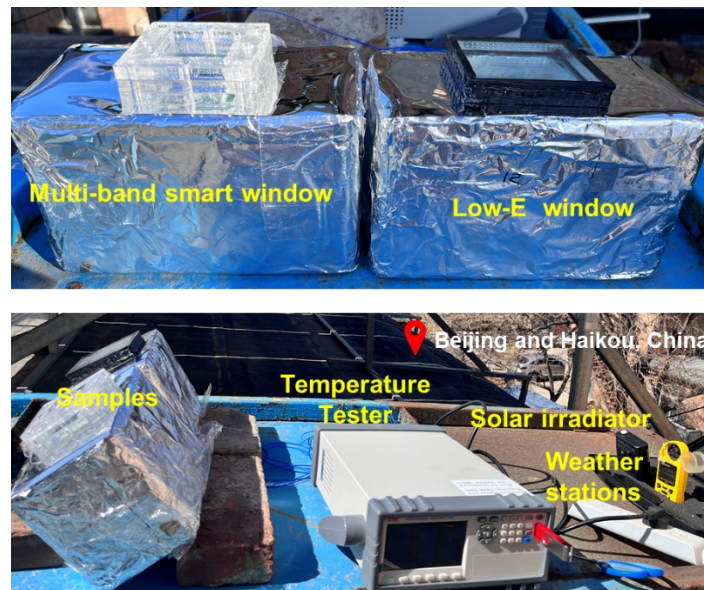
Supplementary Fig. S38. The simulation of the cooling/warming performance of a house using LF-ESWs *vs*. low-E glass-based windows by normalized tests at Beijing, China, and Haikou, China, respectively.
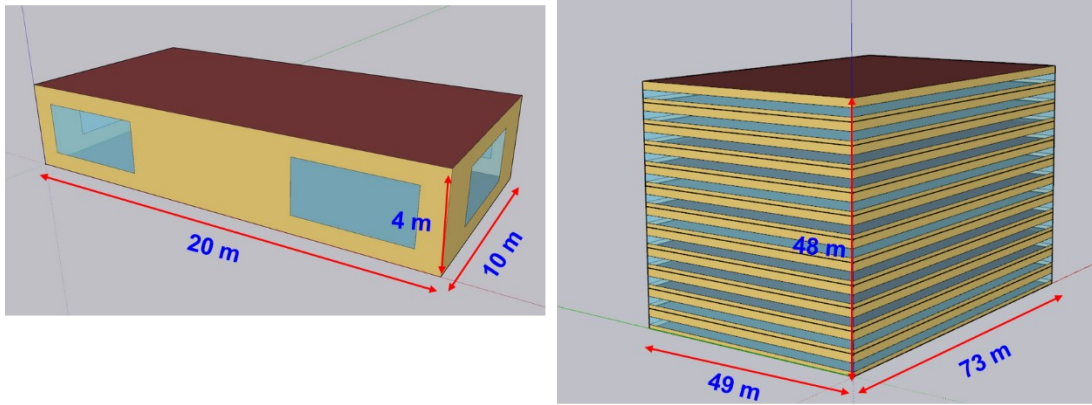
Supplementary Fig. S39. A one-layer model and a twelve-layer model to simulate the energy consumption by EnergyPlus.

Supplementary Fig. S40. The eight cities of eight different climate zones. The software EnergyPlus was used to calculate the all-year-round building energy-saving capabilities of the LF-ESWs in different regions.
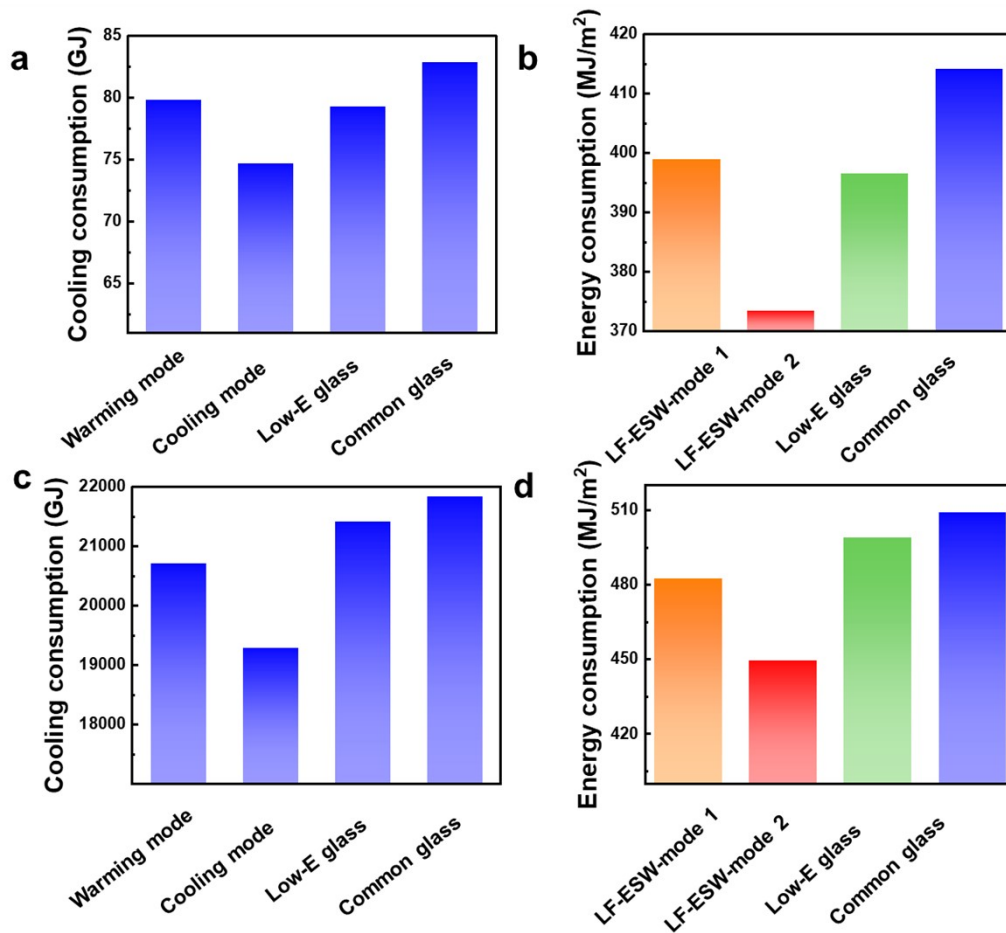
Supplementary Fig. S41. The simulation of the actual energy consumption of (a-b) a one-story model (window-to-wall ratio: 30%) and (c-d) a twelve-story model (window-to-wall ratio: 40%) in Singapore (Zone 1) based on EnergyPlus. LF-ESW-mode 1=heating mode (=0) + warming mode, LF-ESW-mode 2=heating mode (=0) +cooling mode.
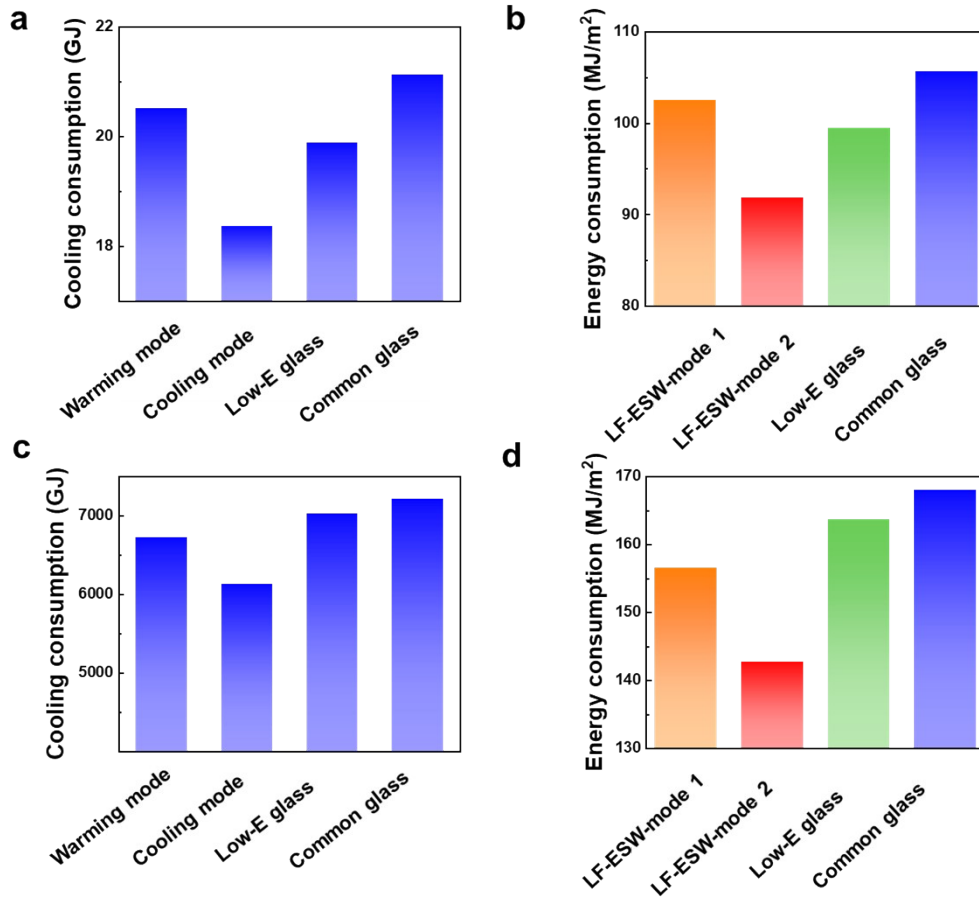
Supplementary Fig. S42. The simulation of the actual energy consumption of (a-b) a one-story model (window-to-wall ratio: 30%) and (c-d) a twelve-story model (window-to-wall ratio: 40%) in Rio de Janeiro (Zone 2) based on EnergyPlus. LF-ESW-mode 1=heating mode (=0) + warming mode, LF-ESW-mode 2=heating mode (=0) +cooling mode.
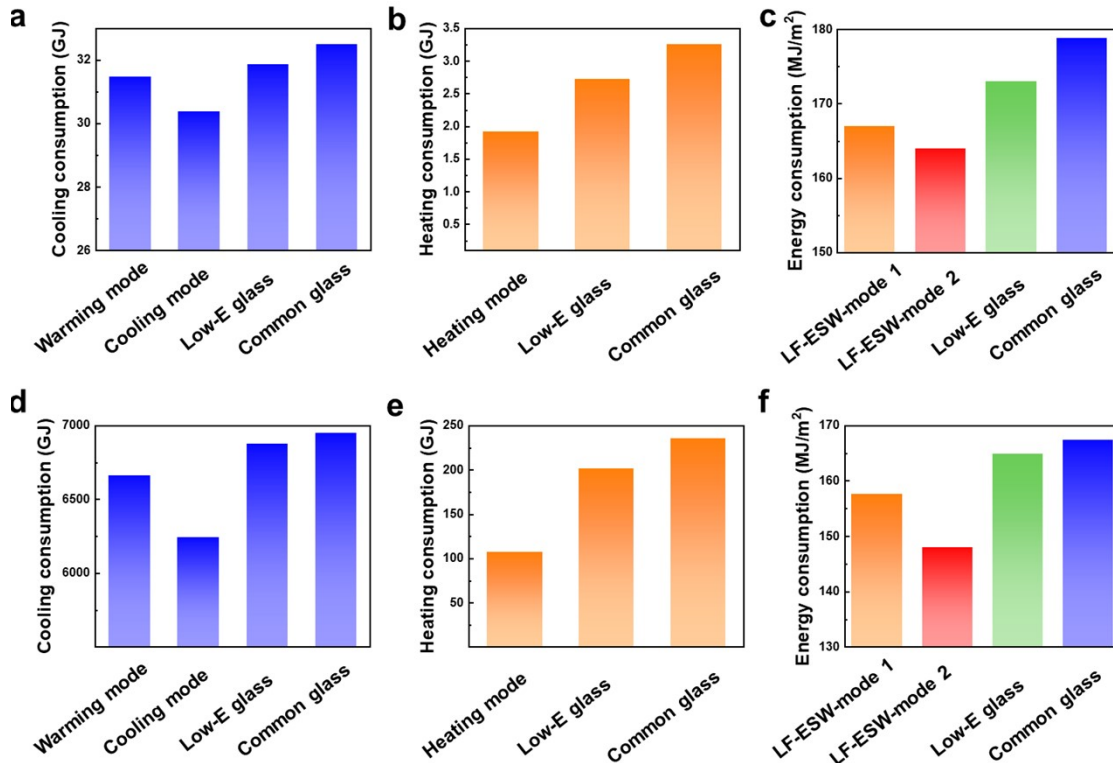
Supplementary Fig. S43. The simulation of the actual energy consumption of (a-c) a one-story model (window-to-wall ratio: 30%) and (d-f) a twelve-story model (window-to-wall ratio: 40%) in Shanghai (Zone 3) based on EnergyPlus. LF-ESW-mode 1=heating mode + warming mode, LF-ESW-mode 2=heating mode + cooling mode.

Supplementary Fig. S44. The simulation of the actual energy consumption of (a-c) a one-story model (window-to-wall ratio: 30%) and (d-f) a twelve-story model (window-to-wall ratio: 40%) in Beijing (Zone 4) based on EnergyPlus. LF-ESW-mode 1=heating mode + warming mode, LF-ESW-mode 2=heating mode + cooling mode.

Supplementary Fig. S45. The simulation of the actual energy consumption of (a-c) a one-story model (window-to-wall ratio: 30%) and (d-f) a twelve-story model (window-to-wall ratio: 40%) in Albuquerque (Zone 5) based on EnergyPlus. LF-ESW-mode 1=heating mode + warming mode, LF-ESW-mode 2=heating mode + cooling mode.
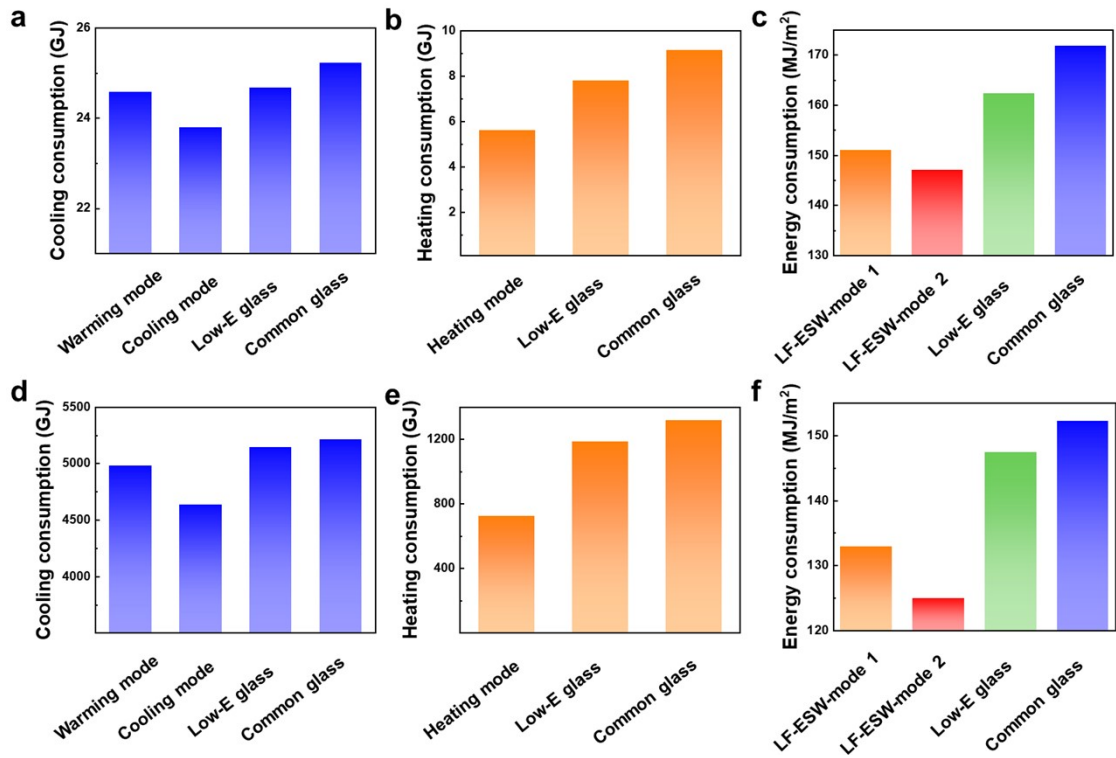
Supplementary Fig. S46. The simulation of the actual energy consumption of (a-c) a one-story model (window-to-wall ratio: 30%) and (d-f) a twelve-story model (window-to-wall ratio: 40%) in Mannheim (Zone 6) based on EnergyPlus. LF-ESW-mode 1=heating mode + warming mode, LF-ESW-mode 2=heating mode + cooling mode.
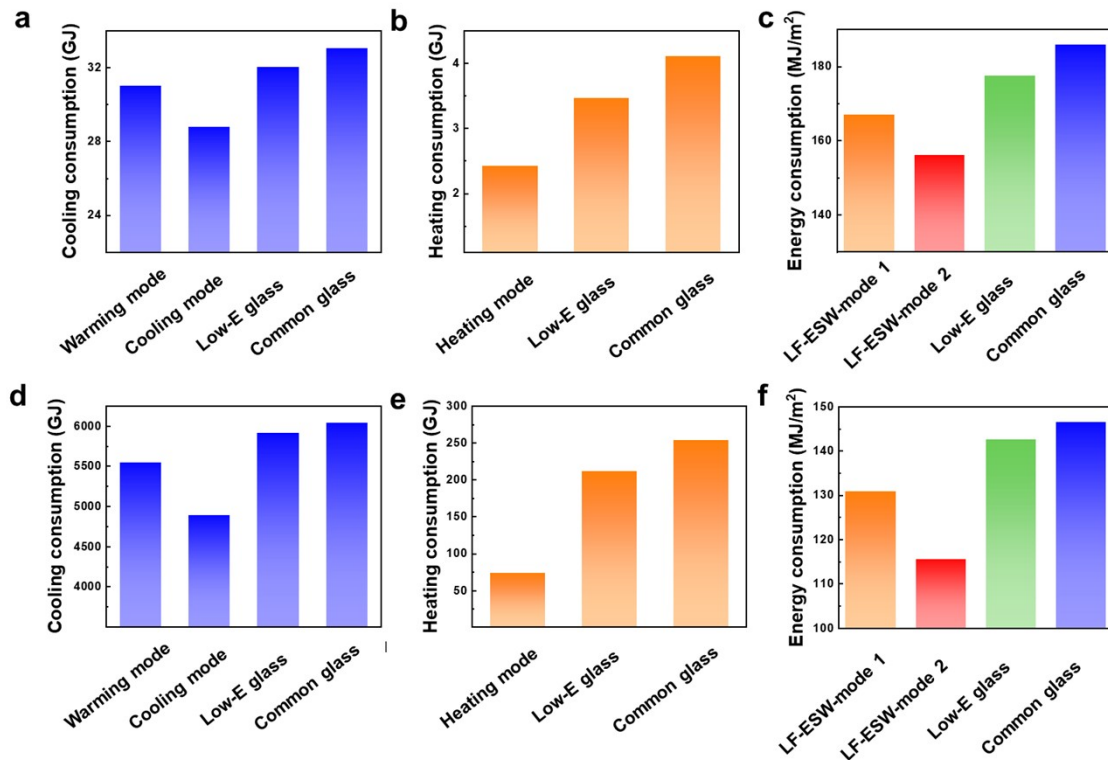
Supplementary Fig. S47. The simulation of the actual energy consumption of (a-c) a one-story model (window-to-wall ratio: 30%) and (d-f) a twelve-story model (window-to-wall ratio: 40%) in Stockholm (Zone 7) based on EnergyPlus. LF-ESW-mode 1=heating mode + warming mode, LF-ESW-mode 2=heating mode + cooling mode.
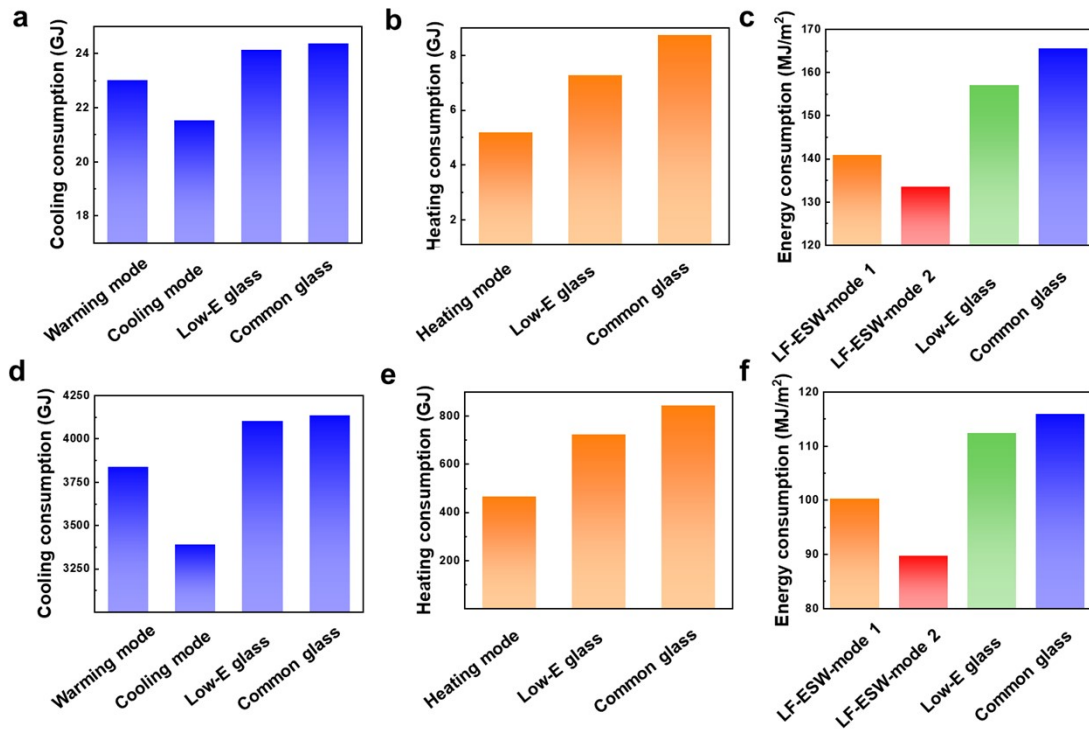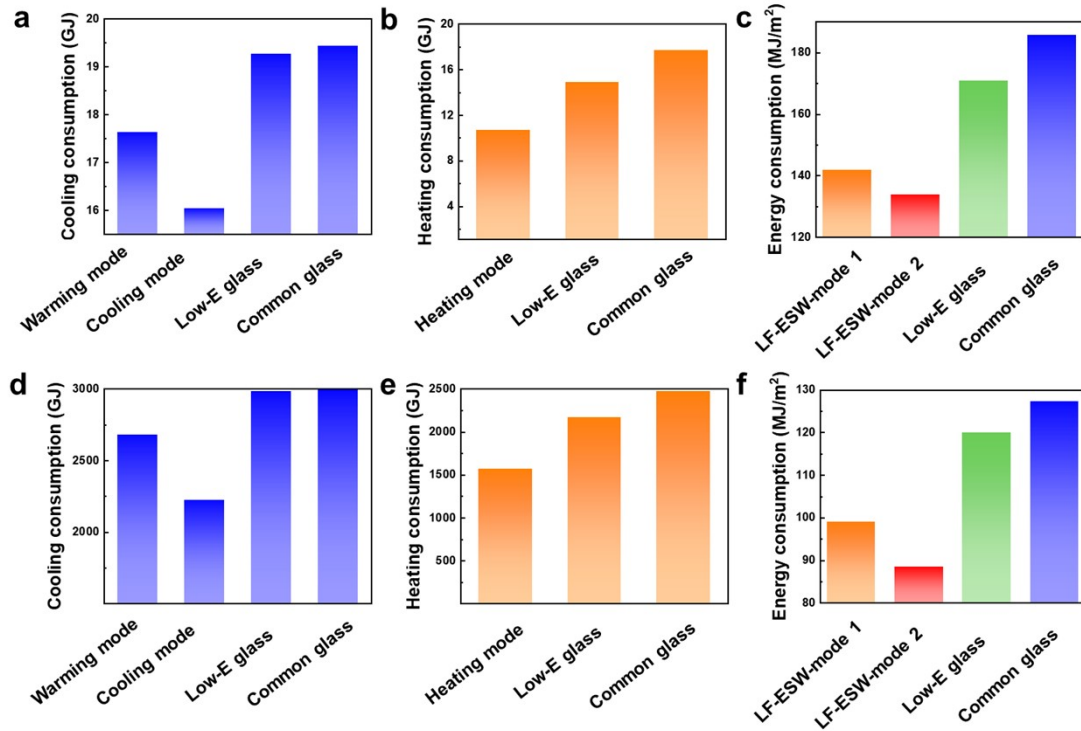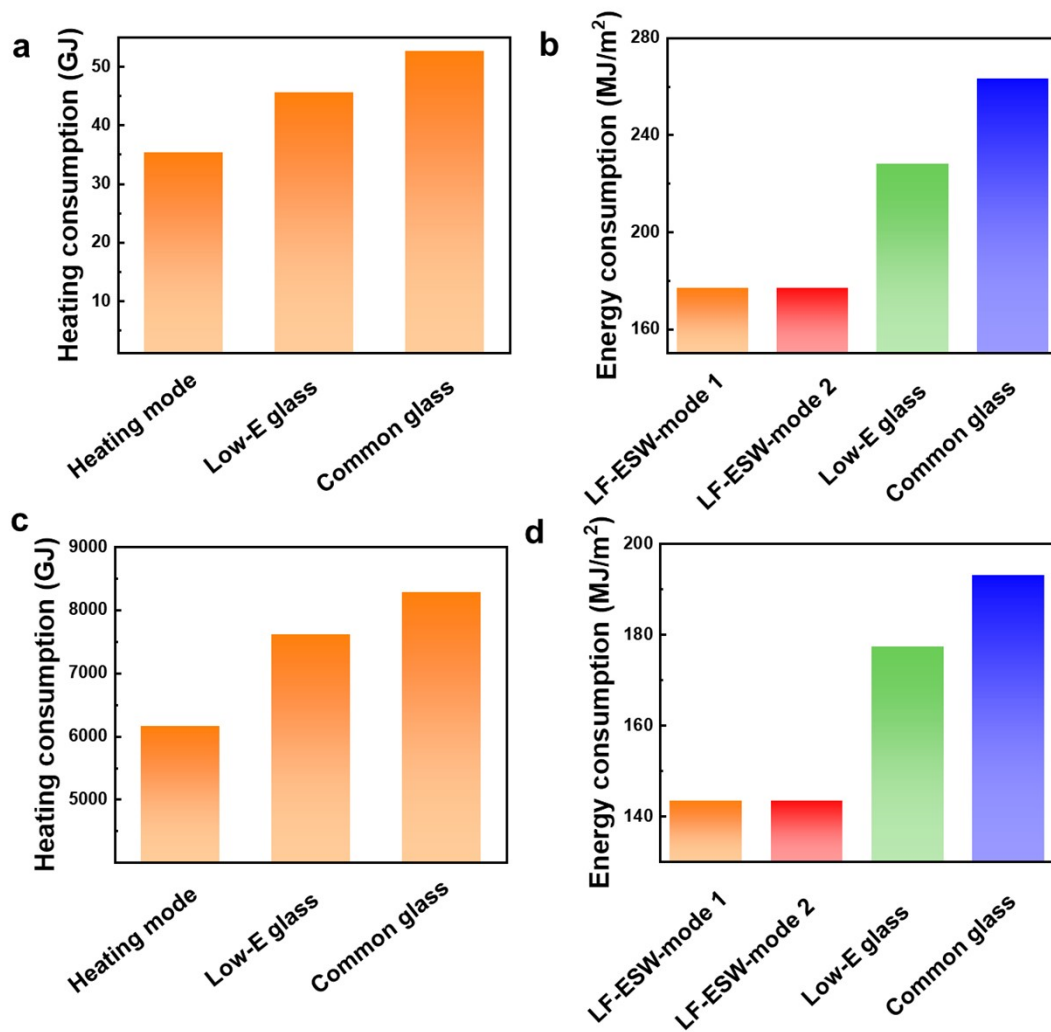
Supplementary Fig. S48. The simulation of the actual energy consumption of (a-b) a one-story model (window-to-wall ratio: 30%) and (c-d) a twelve-story model (window-to-wall ratio: 40%) in Whitehorse (Zone 8) based on EnergyPlus. LF-ESW-mode 1=heating mode + warming mode (=0), LF-ESW-mode 2=heating mode + cooling mode (=0).
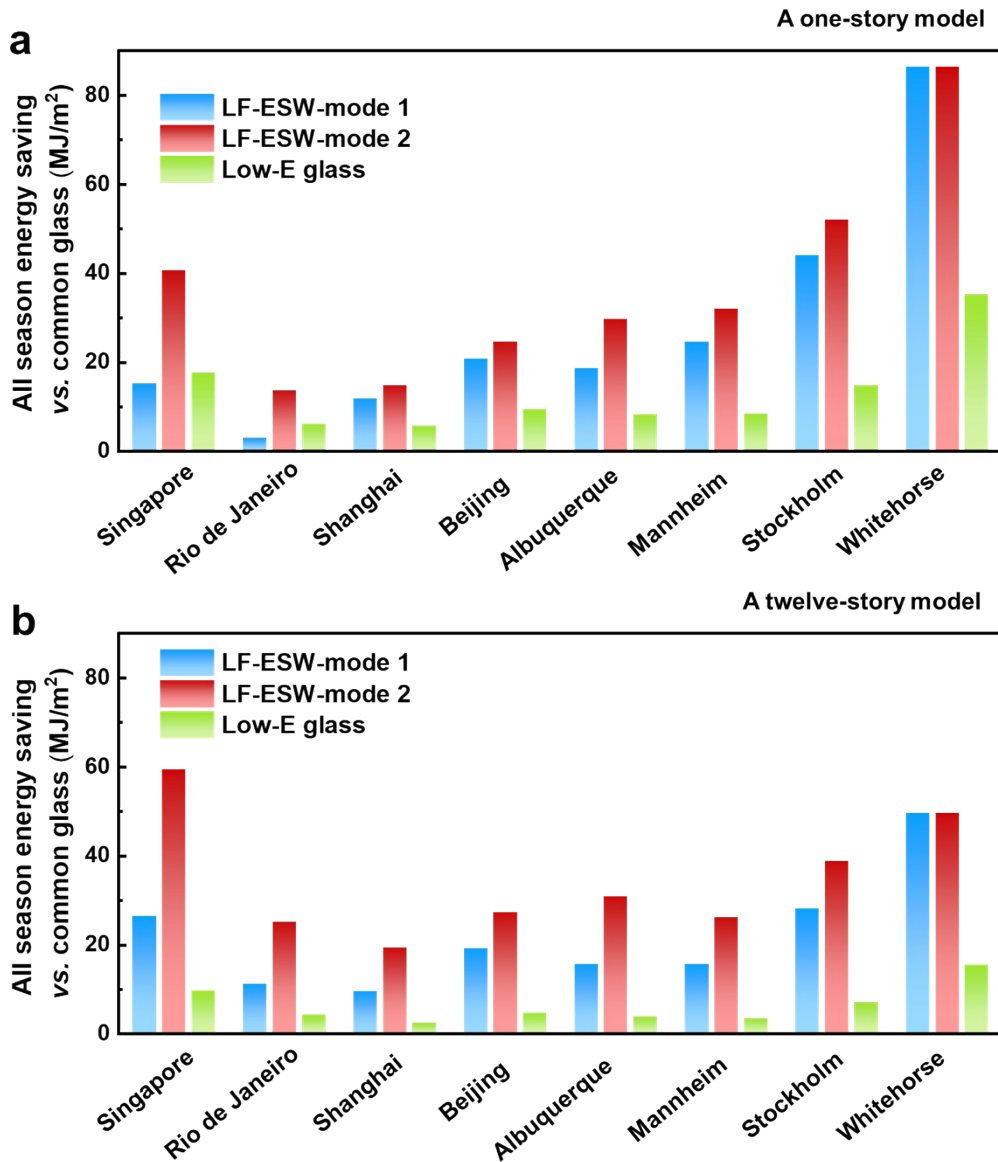
Supplementary Fig. S49. Combined heating and cooling energy consumption of LF-ESWs *vs.* common glass-based windows in eight regions. LF-ESW-mode 1=heating mode+ warming mode, LF-ESW-mode 2=heating mode +cooling mode.
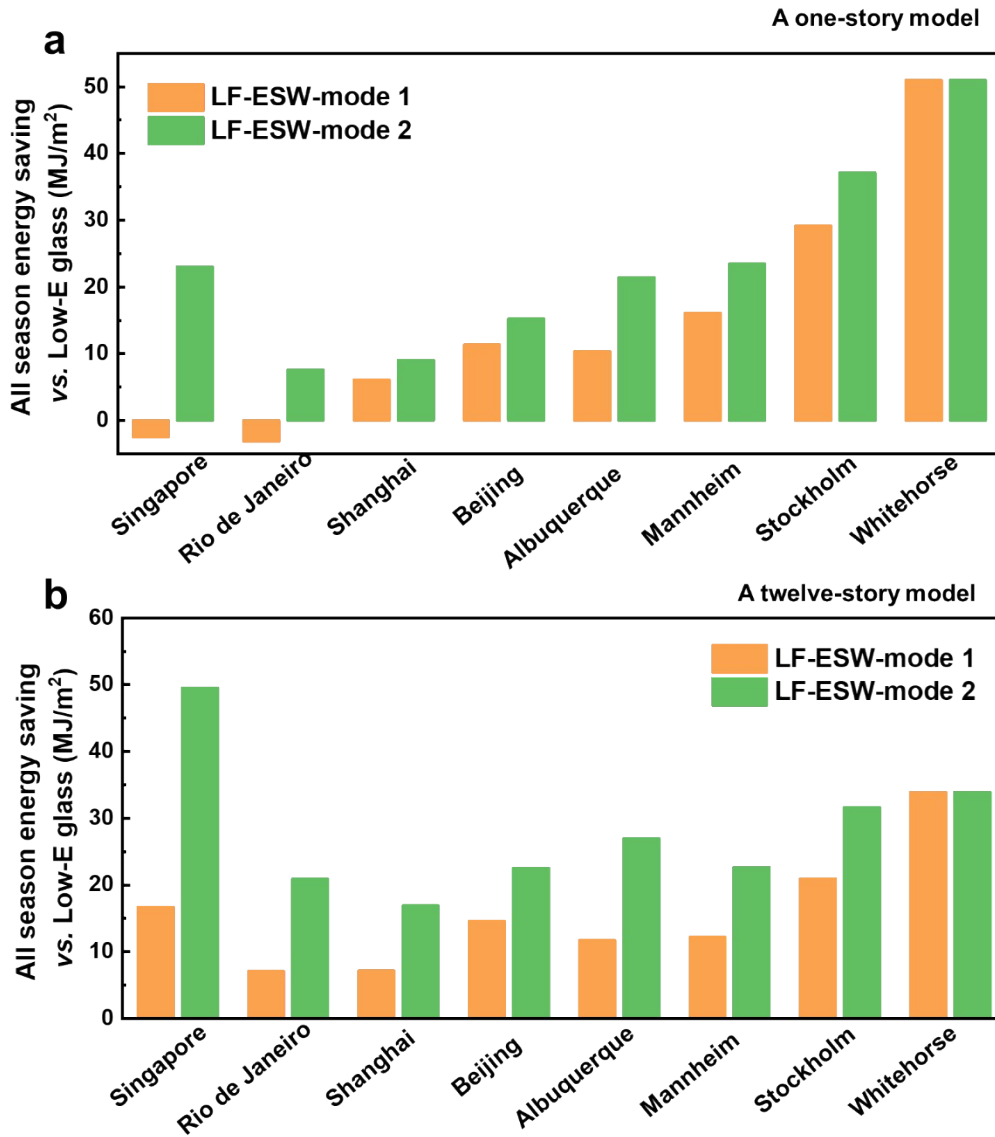
Supplementary Fig. S50. Combined heating and cooling energy consumption of multi-band smart windows *vs*. Low-E windows in eight regions. LF-ESW-mode 1=heating mode+ warming mode, LF-ESW-mode 2=heating mode +cooling mode.

Supplementary Table S1. Building model and related parameter setting for simulation.

parameter	setting
Indoor load	occupancy density: 10 m^2 /person lighting power density: 9 W/ m^2 equipment power density: 15 W/ m^2
Working schedule	8:00 to 18:00 from Monday to Friday
Design parameter	The heating and air conditioning temperatures in the room were set to 20 °C and 24 °C
Lighting control	Linear/off strategy, target illuminance at 300 lx
Equipment for HVAC	Heat pumps are used for heating and cooling, both with COP (coefficient of performance) 2.5

Supplementary Table S2. Requirements for average transmittance ($T_{VIS+NIR}$) of the solar band (0.4~2.5 μm) and the average emissivity (ε_{MIR}) in the atmospheric window band (8~13 μm) of energy-saving windows in six cities with four seasons.

Cities	Season	Energy consumption of common windows (kWh/m^2)	Minimum energy consumption achieved by energy-saving windows (kWh/m^2)	The tipping point to start saving energy		Maximum value of energy saving		Effective scope of regulation
				$T_{VIS+NIR}$	ε_{MIR}	$T_{VIS+NIR}$	ε_{MIR}	$\Delta T_{VIS+NIR}$ and $\Delta\varepsilon_{MIR}$
Beijing	Summer	62.40	52.94	0.659	0.905	0.356	0.999	$0.356<\Delta T_{VIS+NIR}<0.659$ $0.905<\Delta\varepsilon_{MIR}<0.999$
	Winter	28.74	21.44	0.494	0.256	0.684	0.001	$0.494<\Delta T_{VIS+NIR}<0.684$ $0.001<\Delta\varepsilon_{MIR}<0.256$
Munich	Summer	32.50	21.28	0.661	0.905	0.318	0.999	$0.318<\Delta T_{VIS+NIR}<0.661$ $0.905<\Delta\varepsilon_{MIR}<0.999$
	Winter	57.47	49.16	0.454	0.273	0.684	0.001	$0.454<\Delta T_{VIS+NIR}<0.684$ $0.001<\Delta\varepsilon_{MIR}<0.273$
Chicago	Summer	53.22	41.73	0.650	0.909	0.333	0.999	$0.333<\Delta T_{VIS+NIR}<0.650$ $0.909<\Delta\varepsilon_{MIR}<0.999$
	Winter	47.66	40.73	0.476	0.065	0.684	0.001	$0.476<\Delta T_{VIS+NIR}<0.684$ $0.001<\Delta\varepsilon_{MIR}<0.065$
Toronto	Summer	35.27	26.21	0.661	0.905	0.331	0.999	$0.331<\Delta T_{VIS+NIR}<0.661$ $0.905<\Delta\varepsilon_{MIR}<0.999$

City	Season							Range
	Winter	65.70	57.37	0.544	0.235	0.684	0.001	$0.544 < \Delta T_{VIS+NIR} < 0.684$ $0.001 < \Delta \varepsilon_{MIR} < 0.235$
Paris	Summer	40.30	27.58	0.661	0.905	0.319	0.999	$0.319 < \Delta T_{VIS+NIR} < 0.661$ $0.905 < \Delta \varepsilon_{MIR} < 0.999$
	Winter	35.43	30.28	0.438	0.280	0.684	0.001	$0.438 < \Delta T_{VIS+NIR} < 0.684$ $0.001 < \Delta \varepsilon_{MIR} < 0.280$
	Summer	51.82	40.57	0.659	0.905	0.346	0.999	$0.346 < \Delta T_{VIS+NIR} < 0.659$ $0.905 < \Delta \varepsilon_{MIR} < 0.999$
Tokyo	Winter	15.17	10.89	0.494	0.256	0.684	0.001	$0.494 < \Delta T_{VIS+NIR} < 0.684$ $0.001 < \Delta \varepsilon_{MIR} < 0.256$

Supplementary Table S3. Comparison of the performance of the prepared multi-band smart window with the currently reported works.

Strategy	Publication	Working principle	Dynamic control of solar transmittance or not	Transmittance Tunable range	Transmittance tunable contrast	Dynamic control of infrared emissivity or not	Emissivity Tunable range	Emissivity Tunable contrast
VO$_2$[11]	Science	Thermal phase change	Yes	0.3 to 2.5 µm	~10%	Yes	0.21 to 0.61 (2.5 to 25 µm)	0.4
W$_x$V$_{1-x}$O$_2$[12]	Science	Thermal phase change	No	N/A	N/A	Yes	0.2 to 0.9 (8-13 µm)	0.7
Hydrogel[13]	Science Advances	Thermal phase change	Yes	0.3 to 2 µm	58.4%	Yes	0.352 to 0.923 (2.5–16 µm)	0.57
Graphene #1[14]	Nature Photonics	Electrical ion intercalation	No, the transmittance of the reflective device was 0	N/A	N/A	Yes	0.25 to 0.7 (10 µm)	0.45
Graphene #2[15]	Nano Letters	Electrical ion intercalation	No, the transmittance of the reflective device was 0	N/A	N/A	Yes	0.33 to 0.76 (10 µm)	0.43

Multiwalled carbon nanotubes[16]	Advanced Optical Materials	Electrical ion intercalation	No, the transmittance of the reflective device was 0	N/A	N/A	Yes	0.15 to 0.7	0.55
Conductive polymer[17]	Journal of Applied Polymer Science	Electrochromic	No, the transmittance of the reflective device was 0	N/A	N/A	Yes	0.237 to 0.751 (2.5–45 μm)	0.514
PANI[18]	Solar Energy Materials and Solar Cells	Electrochromic	No, the transmittance of the reflective device was 0	N/A	N/A	Yes	2.5 to 25 μm	0.315
Quantum wells[19]	Nature Materials	Electrical ion intercalation	No, the transmittance of reflective device was 0	N/A	N/A	Yes	0.74 to 0.24 (2.5 to 25 μm)	0.5
Electrodeposit Ag[20]	Science Advances	Electrodeposition	No, the transmittance of reflective device was 0	N/A	N/A	Yes	0.08 to 0.79 (7.5 to 13 μm)	0.71
Electrodeposit Cu[21]	Nature Sustainability	Electrodeposition	No, the transmittance of reflective device was 0	N/A	N/A	Yes	0.07 to 0.92 (7.5 to 13 μm)	0.85
Liquid crystal films[22]	Advanced Functional Materials	Electric phase change	Yes	0.3 to 2.5μm	67.2%	No, it's not the dynamic device	0.926 (8 to 14 μm)	0

AZO[23]	Nature Communications	Electrical ion intercalation	No	84.7% (0.4 to 0.76 nm	0	Yes	7.5 to 13 μm	0.41
Li$_4$Ti$_5$O$_{12}$[24]	Advanced Functional Materials	Electrical ion intercalation	No, the transmittance of the reflective device was 0	N/A	N/A	Yes	8 to 13 μm	0.3
This work		Electrochromic and gravity	Yes	0.4 to 2.0 μm	43.53%	Yes	8 to 13 μm	0.74

Supplementary reference

1. X. Wu, J. Li, Q. Jiang, W. Zhang, B. Wang, R. Li, S. Zhao, F. Wang, Y. Huang, P. Lyu, Y. Zhao, J. Zhu and R. Zhang, *Nat. Sustain.*, 2023, **6**, 1446-1454.

2. X. Duan, J. Deng, X. Wang, G. Jinshan and P. Liu, *J. Hazard. Mater.*, 2016, **312**.

3. N. Sharma, A. Singh, N. Kumar, A. Tiwari, M. Lal and S. Arya, *J. Mater. Sci.*, 2024, **59**, 6206-6244.

4. F. Ali, A. Dawood, A. Hussain, N. A. Koka, M. A. Khan, M. I. Khan, M. Asim, N. K. Janjua, M. H. Nasir, Z. Jabeen and F. Zaheer, *Inorg. Chem. Commun.*, 2024, **161**, 112077.

5. P. Shi, S. Fang, D. Luo, L. Yang and S.-i. Hirano, *J. Electrochem. Soc.*, 2017, **164**, A1991.

6. Z. Xu, X. Zhang, J. Yang, X. Cui, Y. Nuli and J. Wang, *Nat. Commun.*, 2024, **15**, 9856.

7. M. Li, R. P. Hicks, Z. Chen, C. Luo, J. Guo, C. Wang and Y. Xu, *Chem. Rev.*, 2023, **123**, 1712-1773.

8. M. Deepa, N. Sharma, S. A. Agnihotry and R. Chandra, *J. Mater. Sci.*, 2002, **37**, 1759-1765.

9. X. Qiu, N. Wang, X. Dong, J. Xu, K. Zhou, W. Li and Y. Wang, *Angew. Chem. Int. Ed.*, 2021, **60**, 21025-21032.

10. Q. Wang, S. Cao, Q. Meng, K. Wang, T. Yang, J. Zhao and B. Zou, *Mater. Horiz.*, 2023, **10**, 960-966.

11. S. Wang, T. Jiang, Y. Meng, R. Yang, G. Tan and Y. Long, *Science*, 2021, **374**, 1501-1504.

12. K. Tang, K. Dong, J. Li, M. P. Gordon, F. G. Reichertz, H. Kim, Y. Rho, Q. Wang, C.-Y. Lin, C. P. Grigoropoulos, A. Javey, J. J. Urban, J. Yao, R. Levinson and J. Wu, *Science*, 2021, **374**, 1504-1509.

13. C. Lin, J. Hur, C. Y. H. Chao, G. Liu, S. Yao, W. Li and B. Huang, *Sci. Adv.*, **8**, eabn7359.

14. M. S. Ergoktas, G. Bakan, E. Kovalska, L. W. Le Fevre, R. P. Fields, P. Steiner,

X. Yu, O. Salihoglu, S. Balci, V. I. Fal'ko, K. S. Novoselov, R. A. W. Dryfe and C. Kocabas, *Nat. Photonics*, 2021, **15**, 493-498.

15. O. Salihoglu, H. B. Uzlu, O. Yakar, S. Aas, O. Balci, N. Kakenov, S. Balci, S. Olcum, S. Süzer and C. Kocabas, *Nano Lett.*, 2018, **18**, 4541-4548.

16. Y. Sun, H. Chang, J. Hu, Y. Wang, Y. Weng, C. Zhang, S. Niu, L. Cao, Z. Chen, N. Guo, J. Liu, J. Chi, G. Li and L. Xiao, *Adv. Opt. Mater.*, 2021, **9**, 2001216.

17. P. Chandrasekhar, B. J. Zay, D. Lawrence, E. Caldwell, R. Sheth, R. Stephan and J. Cornwell, *J.Appl. Poly. Sci.*, 2014, **131**.

18. X. Zhang, Y. Tian, W. Li, S. Dou, L. Wang, H. Qu, J. Zhao and Y. Li, *Sol. Energy Mater. Sol. Cells*, 2019, **200**, 109916.

19. T. Inoue, M. D. Zoysa, T. Asano and S. Noda, *Nat. Mater.*, 2014, **13**, 928-931.

20. M. Li, D. Liu, H. Cheng, L. Peng and M. Zu, *Sci. Adv.*, 2020, **6**, eaba3494.

21. C. Sui, J. Pu, T.-H. Chen, J. Liang, Y.-T. Lai, Y. Rao, R. Wu, Y. Han, K. Wang, X. Li, V. Viswanathan and P.-C. Hsu, *Nat. Sustain.*, 2023, **6**, 428-437.

22. Y. Deng, Y. Yang, Y. Xiao, H.-L. Xie, R. Lan, L. Zhang and H. Yang, *Adv. Funct. Mater.*, 2023, **33**, 2301319.

23. Y. Jia, D. Liu, D. Chen, Y. Jin, C. Chen, J. Tao, H. Cheng, S. Zhou, B. Cheng, X. Wang, Z. Meng and T. Liu, *Nat. Commun.*, 2023, **14**, 5087.

24. J. Mandal, S. Du, M. Dontigny, K. Zaghib, N. Yu and Y. Yang, *Adv. Funct. Mater.*, 2018, **28**, 1802180.